Ore Geology Reviews 124 (2020) 103644

Contents lists available at ScienceDirect

Ore Geology Reviews

journal homepage: www.elsevier.com/locate/oregeorev

The role of early sulfide saturation in the formation of the Yulong porphyry Cu-Mo deposit: Evidence from mineralogy of sulfide melt inclusions and platinum-group element geochemistry

Ming-Liang Huang, Jian-Feng Gao*, Xian-Wu Bi, Lei-Luo Xu, Jing-Jing Zhu, Da-Peng Wang

State Key Laboratory of Ore Deposit Geochemistry, Institute of Geochemistry, Chinese Academy of Sciences, Guiyang 550081, PR China

ARTICLE INFO

Keywords:
Yulong porphyry Cu deposit
Sulfide melt inclusions
Early sulfide saturation
Platinum group elements

ABSTRACT

Sulfide melt inclusions enclosed in silicate minerals have been observed in many oxidized Cu-bearing porphyries. The origin of such sulfide melt inclusions could bear critical information of metal enrichment or depletion during magma evolution of porphyry systems. The giant Yulong porphyry Cu-Mo deposit in eastern Tibetan Plateau consists of a series of felsic intrusions, among which the mineralized Yulong intrusion emplaced at a late stage of the magmatic activity. This study reports detailed texture and composition of sulfide melt inclusions from barren and mineralized intrusions, as well as platinum-group elements of these intrusions, to evaluate potential role of early sulfide saturation in the porphyry mineralization system. These sulfide melt inclusions, occurring as globules or droplets, are preserved in zircon, amphibole and quartz grains. Most of them are composed of a major phase of pyrrhotite and minor pyrite, chalcopyrite and pentlandite. Smooth boundaries between these phases suggest the origin of fractionation from sulfide melt upon cooling. Small amounts of Cu and Ni are heterogeneously distributed in the pyrrhotite. The sulfide melt inclusions could be observed in both the pre- and syn-mineralization intrusions at Yulong, indicating that sulfide saturation had commonly occurred during magma evolution. Magnetite mineral inclusions could be observed in zircon and amphibole grains as well. The mineral assemblage of magnetite + pyrrhotite + pyrite of the mineral inclusions constrains the Yulong magmatic system to redox conditions near the magnetite-pyrite/pyrrhotite buffer and above the fayalite/magnetite-quartz buffer (FMQ). High Eu/Eu* values (0.56–0.78) of the hosting zircons and high calculated ΔNNO values (> 0.5) of the hosting amphibole indicate highly oxidized nature of the parental magma.

Both pre- and syn-mineralization intrusions have low PGE contents (Pt = 0.04 to 0.17 ppb, Pd = 0.19–0.60 ppb) with compositions plotting in the Au-poor porphyry Cu fields in discriminating diagrams. Early sulfide saturation may have been reached and small amounts of sulfides have been segregated from magma. Most PGEs and Au but little Cu have been removed from the evolved magma because the partition coefficient of Cu between sulfide and silicate melt is about two orders of magnitude lower than PGE or Au. As a consequence, the evolved magma would have high Cu but very low PGE and Au, resulting in the Au-poor porphyry Cu mineralization at Yulong.

1. Introduction

Sulfide melt inclusions (SMIs) have been widely observed in silicate phenocrysts (e.g., plagioclase, amphibole) in relatively oxidized ore-forming porphyry systems (Keith et al., 1997; Halter et al., 2005; Stavast et al., 2006; Zhang and Audétat, 2017; Cao et al., 2018; Lowczak et al., 2018). It remains enigmatic as to the origin and role of these SMIs in ore-forming processes. Some authors considered that early sulfide saturation is an indispensable step for porphyry Cu mineralization, because the Cu-rich sulfides could be remobilized during later magmatic-hydrothermal processes and therefore would be favorable to porphyry Cu mineralization (Keith et al., 1997; Halter et al., 2005; Nadeau et al., 2010; Lee et al., 2012; Wilkinson, 2013; Mungall et al., 2015). Some other authors, however, argued that partitioning of metals from the oxidized magma to ore-forming fluids is the dominant mechanism for porphyry Cu mineralization and early sulfide saturation would remove ore-forming metals from the magma and thus decrease the metallogenic potential (Richards, 2003, 2011, 2015; Jugo et al., 2005; Audétat and Pettke, 2006). However, few cases of the mineralogy and compositions of the SMIs are documented in detail so that the role

* Corresponding author.
E-mail address: gaojianfeng@mail.gyig.ac.cn (J.-F. Gao).

https://doi.org/10.1016/j.oregeorev.2020.103644
Received 31 December 2019; Received in revised form 24 May 2020; Accepted 8 June 2020
Available online 11 June 2020

of early sulfide saturation in porphyry Cu mineralization is still unclear.

The giant Yulong porphyry Cu-Mo deposit in eastern Tibetan Plateau is the third largest Cu deposit in China (Yang and Cooke, 2019). It is a Cu and Mo-rich, Au-poor porphyry deposit, with the Cu-Mo mineralization temporally and spatially related to the Yulong intrusion that was emplaced at about 41.0 Ma (Tang and Luo, 1995; Guo et al., 2006; Hou et al., 2006; Liang et al., 2006; Tang et al., 2009; Li et al., 2012; Huang et al., 2019a). Aside from the intensively mineralized Yulong intrusion, the Yulong ore district also hosts a series of pre-mineralization subeconomic intrusions (Guo et al., 2006; Jiang et al., 2006; Wang et al., 2011; Huang et al., 2019a). We have observed some SMIs that are enclosed by magmatic zircons as well as amphibole and quartz phenocrysts from these intrusions, indicating that the Yulong magmatic suite has reached sulfide saturation in early stage of magma evolution. Thus, the Yulong deposit is ideal for evaluating the role of early sulfide saturation in porphyry mineralization.

In this paper, we present detailed mineralogy and composition of the SMIs in silicate minerals and PGE concentrations of barren and mineralized intrusions. With new dataset we document that parental magmas for the Yulong intrusion had reached sulfide saturation before Cu mineralization. We have also discussed the formation conditions (magmatic oxygen fugacity, temperature and pressure) and the possible role of early sulfide saturation in the formation of the Au-poor Yulong porphyry Cu-Mo deposit.

2. Regional geology

The Cenozoic Jinshajiang-Red River magmatic belt (JSRR) in southwest China stretches over 2000 km from the Qiangtang Terrane in eastern Tibet to the Western Yangtze Craton (Fig. 1A; Zhang and Xie, 1997; Xu et al., 2012,2016). This belt consists of numerous Eocene-Oligocene alkaline volcanic and intrusive rocks (Fig. 1A) and associated porphyry Cu-Mo-Au deposits, such as the Beiya porphyry-skarn Au deposit (Deng et al., 2015; He et al., 2015), the Machangqing porphyry Cu-Mo deposit (Hu et al., 2004; Bi et al., 2005, 2009), and the Yulong porphyry Cu-Mo deposit (Hou et al., 2003; Jiang et al., 2006; Liang et al., 2006; Li et al., 2012; Chang et al., 2017). Ages of magmatism and porphyry Cu mineralization in this belt have been dated at 44–31 Ma (Zhang and Xie, 1997; Liang et al., 2006; Hou et al., 2006; Xu et al., 2012). These alkaline magmatism and porphyry Cu mineralization have widely been considered to be formed in post-subduction strike-slip faulting systems related to India-Asian collision since 65–55 Ma (Zhang and Xie, 1997; Hou et al., 2003; Bi et al., 2005, 2009; Mo et al., 2007; Xu et al., 2012,2016).

The JSRR belt could be subdivided into two magmatic belts, with the southern part being the Ailaoshan belt and the northern part being the Yulong belt (Fig. 1B). The Yulong belt is located in the Qiangtang Terrane, which consists of Proterozoic to early Paleozoic basement, and middle Paleozoic–Mesozoic clastic and carbonate cover rocks as well as Tertiary sedimentary basins (Fig. 1B; Tang and Luo, 1995; Hou et al., 2003). The regional structure is dominated by northwest–southeast strike-slip faults that are part of the strike-slip faulting systems along the JSRR belt. These faults controlled the distribution of the Eocene alkaline porphyry intrusions and related porphyry Cu-Mo-Au deposits within the NW-SE trending Yulong belt (Tang and Luo, 1995; Hou et al., 2003). The Yulong belt is composed of eight Eocene porphyry Cu systems (43.6–37.1 Ma; Fig. 1A-B), four of which have proven Cu reserves of > 0.5 Mt (Yulong: 6.24 Mt, Malasongduo: 1.0 Mt, Duoxiasongduo: 0.5 Mt, and Narigongma: 0.5 Mt; Tang and Luo, 1995; Hou et al., 2003; Liang et al., 2006; Yang et al., 2014). Most recently, the Bada deposit, a Au-Cu deposit genetically associated with Eocene quartz monzonite porphyry, has been discovered in the Yulong belt (Zhang et al., 2019; Jiang and Li, 2019 unpublished oral presentation). This deposit has estimated Au and Cu resources of > 90 t and > 0.36 Mt, respectively (Zhang et al., 2019). These porphyry Cu-Mo-Au systems in the Yulong belt are considered to be formed by partial melting of Paleo-Tethys subduction-modified juvenile crust (Li et al., 2012; Lin et al., 2018; Huang et al., 2019b). The Yulong deposit is the largest one among these deposits, and contains 1048 Mt ores with average grades of 0.62% Cu and 0.041% Mo, respectively (Tibet Yulong Copper Co., Ltd., 2009).

3. Deposit geology

The Yulong porphyry Cu-Mo deposit is located about 80 km west of the town of Jiangda in eastern Tibetan Plateau. Sedimentary rocks in the Yulong ore district comprises of Triassic Jiapila (quartz sandstones and mudstones), Bolila (carbonates interlayered by quartz sandstones) and Adula (shales) formations. Intensive skarn-type Fe-Cu mineralization was developed at the contacts between the Jiapila Formation and the Yulong intrusion. These sedimentary rocks are thought to have contributed parts of the ore-forming materials to the Yulong deposit (e.g. Pb; Huang et al., 2019c). Structures within the Yulong deposit include the SE-pitching Hengxingcuo anticline and the ring-shaped, steeply dipping faults that encircle the Yulong intrusion. The Hengxingcuo anticline is a pre-ore structure caused by regional transpressional strike-slip faults, whereas the ring-shaped faults were formed in response to local compression due to emplacement of the Yulong intrusion (Tibet Yulong Copper Co., Ltd., 2009).

Copper and Mo mineralization are genetically associated with and spatially hosted in the Yulong intrusion, which consists of three successive porphyry phases (Chang et al., 2017). The earliest phase, the majority of the Yulong intrusion, is composed of monzogranite porphyry (MGP) that has mineral assemblage of quartz + plagioclase + K-feldspar + amphibole + biotite and accessory minerals such as apatite, titanite, zircon and magnetite. Emplacement age of the MGP has been dated (zircon U-Pb ages, 2σ) from 42.0 Ma to 40.9 Ma (Guo et al., 2006; Liang et al., 2006; Wang et al., 2009; Li et al., 2012; Chang et al., 2017; Huang et al., 2019a). The MGP is syn-mineralization and has experienced extensive potassic alteration, which is expressed by secondary K-feldspar and biotite, and various kinds of quartz + molybdenite + chalcopyrite ± biotite veins (Fig. 3). > 80% of the Cu and Mo mineralization at Yulong was produced by this phase (Chang et al., 2017). The second phase is a K-feldspar porphyry (KGP; Fig. 3). It occurs as small dikes intruding the MGP, and has similar mineral assemblage to the MGP. The KGP has zircon U-Pb ages of 41.2 Ma (Chang et al., 2017), which is indistinguishable from the MGP. Small proportion of Cu and Mo mineralization (~20%) was produced by this phase (Chang et al., 2017). The third phase, the quartz albite porphyry (QAP), is a post-mineralization porphyry that also occurs as small dikes intruding the MGP and KGP (Fig. 3), and yields younger zircon U-Pb age of 40.1 Ma (Chang et al., 2017). It has similar mineral assemblage to the MGP, but are distinguished by less abundant of phenocrysts. The emplacement of the QAP has caused intensive-strong phyllic alteration in the MGP and KGP, but no economic Cu or Mo mineralization was produced. Intensive argillic alteration and supergene mineralization is developed at upper and outer part of the Yulong intrusion, which contains 1.27 Mt Cu at an average grade of 1.31% Cu (Tibet Yulong Copper Co., Ltd., 2009). Although the supergene mineralization zone was previously considered to be Au-rich (Hou et al., 2007), recent exploration shows that this zone (as well as the porphyry-type ores in the potassic alteration zone) has very low Au grade of ~0.054 g/t (Tibet Yulong Copper Co., Ltd., 2009).

There are several pre-mineralization, spatially independent, subeconomic intrusions in the Yulong ore district (Fig. 2), including quartz monzonite porphyry (Y8 and Ganlongla intrusions), monzogranite porphyry (Y1, Y3 and Y7 intrusions) and granodiorite porphyry (Y9 and Y10 intrusions). They have slightly older zircon U-Pb ages (43.9 Ma to 41.4 Ma; Guo et al., 2006; Wang et al., 2009; Huang et al., 2019a), but indistinguishable mineral assemblage, whole-rock geochemistry, and zircon Hf isotopes with the mineralization-related MGP (Jiang et al., 2006; Wang et al., 2011; Li et al., 2012; Huang et al., 2019a), suggesting that these intrusions are co-magmatic. Although the pre-

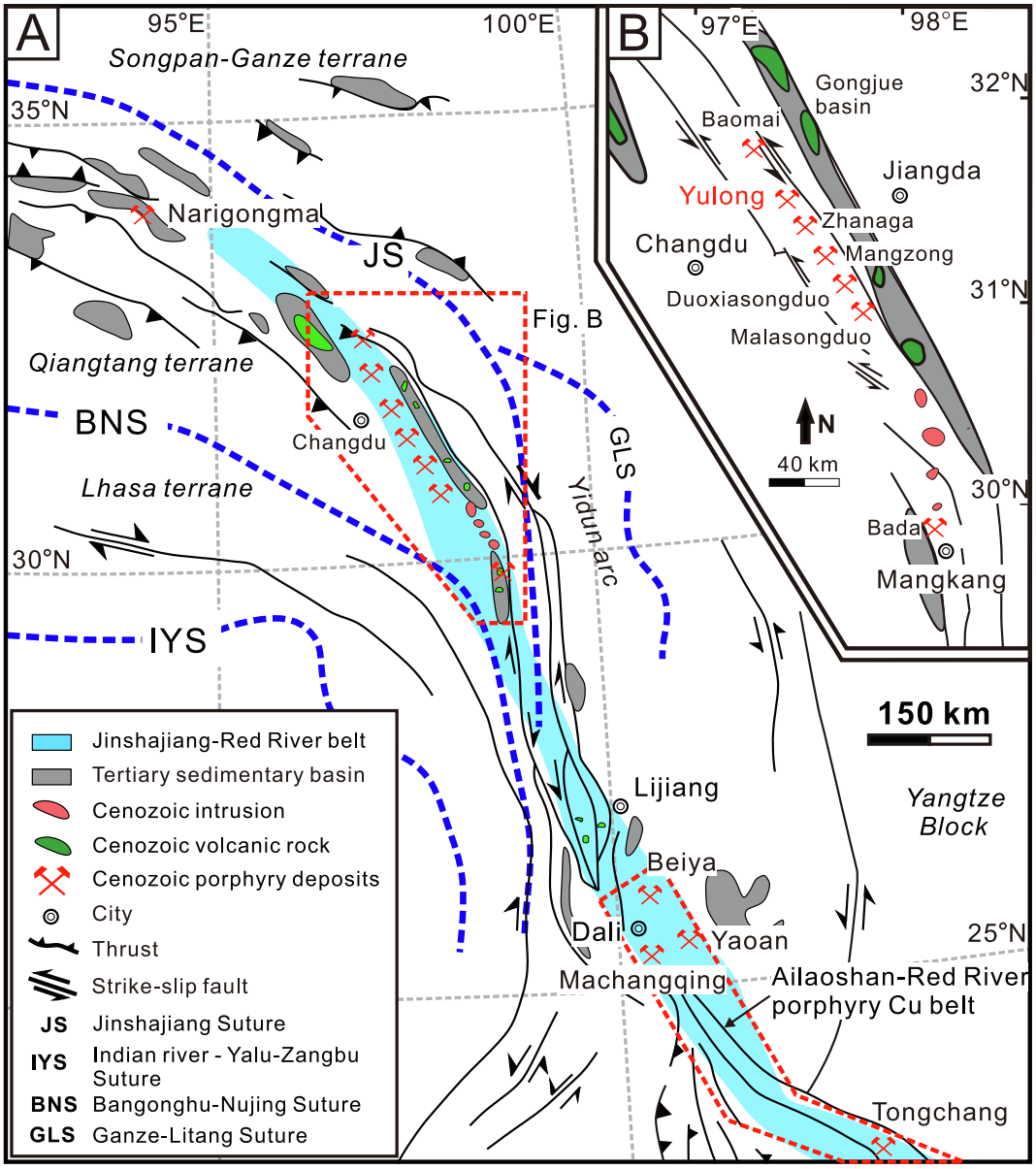

Fig. 1. A. Simplified geological map of the Jinshajiang-Red River porphyry Cu ± Mo ± Au deposit belt (Modified from Wang et al., 2001). B. Simplified geological map of the Yulong porphyry Cu ± Mo deposit belt, showing the distribution of porphyry Cu-Mo deposits (Modified from Hou et al., 2003).

mineralization intrusions have similar magmatic oxidation states and sulfur and water contents with the mineralized MGP, and are therefore fertile for ore-formation, no economic Cu-Mo mineralization has been discovered in these intrusions.

4. Sample description and analytical methods

A total of fifteen SMIs were observed in the syn-mineralization MGP of the Yulong composite porphyry stock (sample ZK0812-389; for convenience, the MGP is referred to as the Yulong intrusion in the following text) and three pre-mineralization subeconomic intrusions (Y1 intrusion: sample YL1636; Y7 intrusion: sample YL1647; Y8 intrusion: sample YL1656) at Yulong. Detailed locations and descriptions of these samples have been given in our previous study (Huang et al., 2019a). Twelve of the observed SMIs are carefully polished to the surface, and are investigated by electron microprobe (EMPA) and scanning electron microscopy-energy dispersive spectrometry (SEM-EDS). Uranium-lead ages and trace element compositions of sulfides-hosting zircons were obtained by LA-ICP-MS analyses. Major element compositions of one sulfide-hosting amphibole were obtained by EMPA. In addition, twelve least-altered samples from the mineralized Yulong intrusion and two samples from pre-mineralization subeconomic intrusions (Y1 and Y3), whose whole-rock major and trace element compositions have been analyzed by Huang et al. (2019a, b), are selected for whole-rock platinum group element analyses.

4.1. Zircon LA-ICP-MS U-Pb dating and trace element analysis

Transmitted and reflected light photographs, as well as back scattered electron (BSE) and cathodoluminescence (CL) images of the sulfide-hosting zircons were taken at the State Key Laboratory of Ore Deposit Geochemistry, Chinese Academy of Sciences (SKLODG, IGCAS) to reveal potential cracks around the SMIs, and to help select suitable spot for LA-ICP-MS. Laser ablation-ICP-MS zircon U-Pb dating and trace element analyses were performed at SKLODG by using a GeoLasPro 193 nm ArF excimer laser equipped with Agilent 7900 ICP-MS. Laser spot size of 32 μm and repetition of 6 Hz were used. Each analysis included a background acquisition of about 20 s (gas blank) followed by

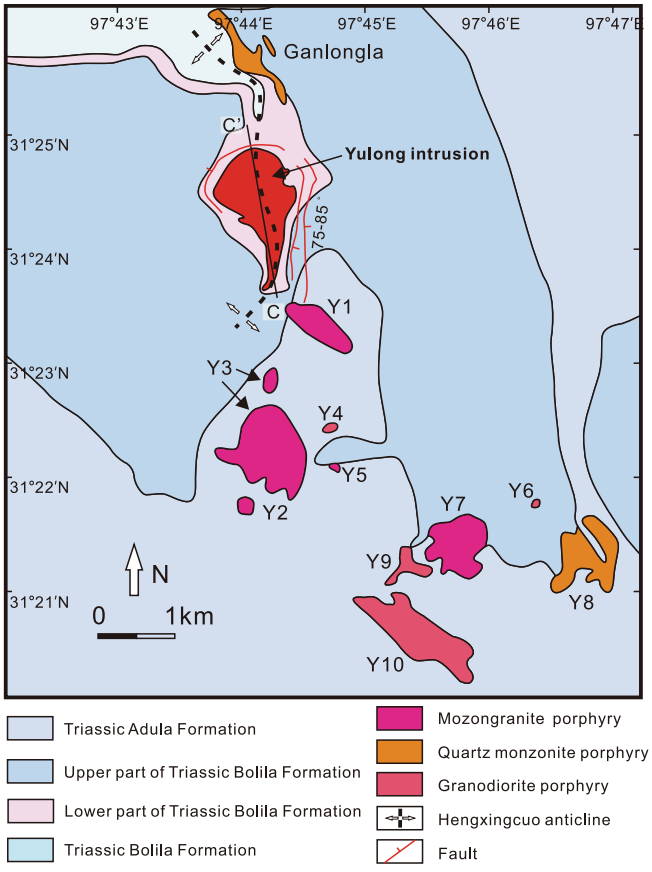

Fig. 2. Geologic map of the Yulong ore district, eastern Tibet, showing sedimentary rocks, structures, and distribution of mineralized and subeconomic intrusions (Modified from unpublished report of the Tibet Yulong Copper Co., Ltd., 2009).

50 s of data acquisition from the sample. Helium was used as the carrier gas, and argon was used as the makeup gas. They were mixed via a T-connector before entering the ICP-MS. Detailed analytical procedure, off-line signal selection and integration and quantitative calibrations can be found in Liu et al. (2008,2010). Zircon 91,500 was used as external standards for U-Pb dating (Wiedenbeck et al., 1995), and NIST 610 was used as external standard for trace element calibrations.

4.2. Quantitative analyses and element mapping of SMIs and amphibole phenocryst

The observed SMIs were first studied under optical microscope, and then analyzed using the JEOL JSM7800F scanning electron microscope (SEM) equipped with Energy-dispersive spectrometer (EDS) at the SKLODG. Compositional data of all the observed SMIs and a sulfide-hosting amphibole phenocryst were acquired by a JXA8530F-plus electron microscope using wavelength-dispersive spectroscopy (WDS) at the SKLODG. For the analyses of SMIs, the conditions are 25 kV accelerating voltage, 10nA beam current, and 0.3–2 μm beam diam. Ten elements (Ag, Au, Mo, Pd, Pt, S, Fe, Cu, Ni, Co) were measured, with only the results of S, Fe, Cu and Ni are above the detection limits (61 ppm, 96 ppm, 114 ppm and 105 ppm, respectively). These SMIs were also applied to WDS mapping to reveal the spatial distribution of S, Fe, Cu, Au, Pd and Ni with an accelerating voltage of 25 kV, beam current of 20nA, and a point dwell time of 10 ms. For the amphibole, twelve elements (Fe, Ca, Ti, Cr, Na, Mg, F, Si, Al, K, Cl and Mn) were measured under the following conditions: 25 kV accelerating voltage, 10nA beam current, and 10 μm beam diam. All data were corrected based on the ZAF procedure.

4.3. Whole-rock platinum-group elements analyses

Whole rock PGE contents were determined by using isotope-dilution ICP-MS (ID-ICP-MS) at Institute of geochemistry, Chinese Academy of Sciences (IGCAS), following the revised Carius tube technique (Qi et al., 2011). About 8 g sample powders were precisely weighted and decomposed in Carius tube with HF and HNO_3. Appropriate amounts of isotope spike solutions of ^{105}Pd, ^{101}Ru, ^{193}Ir, and^{194}Pt were accurately weighted and added into samples. PGEs in decomposed solution were concentrated by Te-coprecipitation. A mixed ion exchange resin of Dowex 50 W-X8 cation exchange and P507 extraction chromatograph resins was used to remove Cu, Ni, Zr, and Hf to minimize possible interference for PGE analyses. Detailed digesting, concentrating and analyzing procedure were described in Qi et al. (2011) and Gao et al. (2015). Pd, Pt, Ir, and Ru were measured by ID-ICP-MS and Rh was measured by using ^{194}Pt as the internal standard. The detection limits are < 0.015 ppb for Pt and Pd and < 0.008 ppb for Ir and Ru (Qi et al., 2011). Total procedural blanks were lower than 0.002 ppb for Ir, 0.003 ppb for Rh, 0.002 ppb for Ru, 0.012 ppb for Pd, and 0.020 ppb for Pt, respectively. Accuracy of the analyses was monitored by using standard material of NRCAN UMT-1 (mill tailings) and TDB-1 (diabase).

5. Results

5.1. Zircon U-Pb ages and trace element compositions

The U-Pb ages and trace element compositions of the six sulfide-hosting zircon crystals are listed in Tables 1 and 2, respectively, and are shown in Fig. 4. They have $^{206}Pb/^{238}U$ ages of 41.9 ± 0.6 Ma to 40.7 ± 0.6 Ma, which are consistent with the reported weighted mean zircon $^{206}Pb/^{238}U$ ages of the Yulong intrusion (Liang et al., 2006; Li et al., 2012; Huang et al., 2019a).

Chondrite-normalized REE patterns of analyzed zircons are characterized by small negative Eu anomalies, positive Ce anomalies, and depletion of light rare earth elements (LREE) relative to heavy rare earth elements (HREE) (not shown). Zircon Eu_N/Eu_N^* values ($Eu_N/Eu_N^* = Eu_N/(Sm_N \times Gd_N)^{0.5}$) vary between 0.56 and 0.78. Titanium-in-zircon temperatures (°C; $T_{Ti\text{-}in\text{-}zircon}$) of these zircons, caculated following the method of Watson et al. (2006), vary from 574° to 714 °C (Table 2). These values are also consistent with the reported values of the Yulong magmatic suite (Huang et al., 2019a).

5.2. Elemental compositions of SMIs

Although all the observed SMIs were analyzed by EPMA, only four of them yielded roughly reliable results with the sum > 96 wt%. We restrict our quantitative results to these four analyses, and apply the semiquantitative results of EDS analyses to the remaining SMIs. The quantitative and semiquantitative results are tabulated in Tables 3 and 4, respectively. The WDS mapping results for representative element (Fe, S, Cu, Au and Ni) are shown in Figs. 8–11. All these SMIs are composed mainly of S, Fe and minor Cu and Ni, and undetectable Mo, Pd and Au (Tables 3–4). Fe:S atom ratios of most SMIs vary between 0.85:1 to 0.96:1, indicating that they are mostly pyrrhotite ($Fe_{1-x}S$, x = 0–0.223, corresponding to Fe:S of 0.777:1 to 1:1). One EDS analysis (Py-YL1636-Zir2) yielded Fe:S atom ratio of 0.57:1 that is different from pyrrhotite, but more closely to that of pyrite. Another EDS analysis (Cpy-ZK0812-389-Zir3) yielded Fe:S:Cu atom ratio of 0.57:1:0.5 that is roughly similar to that of chalcopyrite. Another EDS analysis (Po-YL1656-Zir2) yielded Fe:S:Cu atom ratio of 0.66:1:0.37, respectively. This ratio is different from those of pyrite, pyrrhotite and chalcopyrite. WDS mapping results suggest that rim of this SMI is much more enriched in Cu (Fig. 10 A–B). We speculate that the result of the above EDS analysis was a mixture of the Cu-poor (probably pyrrhotite) and Cu-rich (probably chalcopyrite) zone.

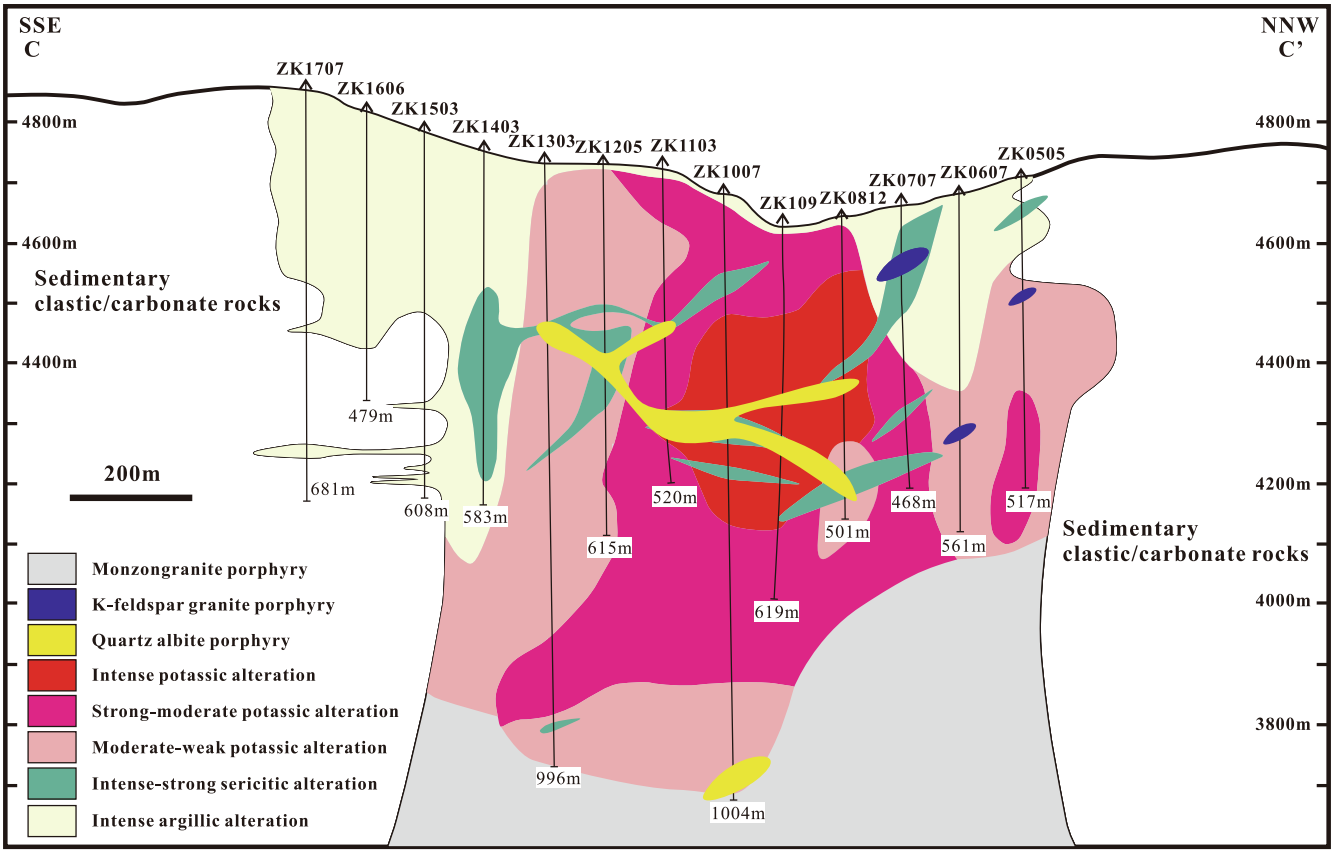

Fig. 3. Schematic cross section of C-C', showing the appearance of multiphase porphyry intrusions and alteration zonation of the Yulong composite porphyry stock. (Modified from Chang et al., 2017; Huang et al., 2019a). Cross section C-C' is shown in Fig. 2.

5.3. Composition of the sulfide-hosting amphibole

Two EMPA analyses were conducted on the same amphibole phenocryst that hosts SMIs. They yielded reproducible results with high Al_2O_3 (11.6 wt%), FeO (12.2 wt% and 12.6 wt%), TiO_2 (2.1 wt%) and low SiO_2 (42.4 wt% and 42.6 wt%) (Table 5). These compositions are used to calculate water contents, temperature, and oxidation states of the magma from which amphibole crystallized. The results show that the parental magma had relatively high water contents (ca. 4 wt%), temperature (ca. 952 °C) and oxygen fugacity (ΔNNO = 0.5, the NNO is the Ni-NiO buffer; Table 5; Fig. 12; Ridolfi et al., 2010).

5.4. Whole-rock platinum-group element compositions

The PGE contents of the samples from Yulong porphyry deposit, as well as those of the standard UMT-1 and TDB-1, are listed in Table 6. The RSD of UMT-1 results are < 8% for Pd and Pt, and < 35% for Ir, Ru and Rh. The uncertainties of Pd, Pt, Ru, Ir, and Rh are 4.4%, 12.4%, 23.3%, 13.3% and 12.8%, respectively, according to the analysis of TDB-1. Samples from the mineralized Yulong intrusion have low Pd and Pt contents ranging from 0.19 to 0.60 ppb (average = 0.32 ± 0.11 ppb) and from to 0.04 to 0.17 ppb (average = 0.11 ± 0.04 ppb), respectively (Fig. 13A–B). Two samples from the pre-mineralized sub-economic intrusions have similarly low Pd (0.33 ppb and 0.53 ppb) and Pt (0.04 ppb and 0.08 ppb).

6. Discussion

6.1. Magmatic origin of the SMIs

Most SMIs in the Yulong deposit are composed of more than one mineral phases. The dominant mineral phase is pyrrhotite that consists of Fe and S with minor Cu and Ni. Cu and Ni are heterogeneously distributed in the pyrrhotite (Figs. 10 and 11). Another major phase occurs as rims surrounding the pyrrhotite (Fig. 10A–B), which is apparently enriched in Cu and is probably chalcopyrite. Another mineral is pentlandite that is extremely enriched in Ni but depleted in Fe and Cu (Fig. 11B). These mineral phases have smooth boundaries, probably

Table 1
LA-ICP-MS U-Pb ages of zircons hosting magmatic sulfide melt inclusions.

			Isotopic ratios						Age (Ma)					
Analyses	Th(ppm)	U(ppm)	$^{207}Pb/^{206}Pb$	1σ	$^{207}Pb/^{235}U$	1σ	$^{206}Pb/^{238}U$	1σ	$^{207}Pb/^{235}U$	1σ	$^{206}Pb/^{238}U$	1σ	$^{208}Pb/^{232}Th$	1σ
YL1636-1	96	156	0.0478	0.0084	0.0413	0.0045	0.0065	0.0003	41.1	4.4	41.7	2.2	53.6	4.9
YL1636-2	272	588	0.0439	0.0074	0.0387	0.0060	0.0064	0.0003	38.6	5.9	41.1	1.7	46.8	4.0
ZK0812-389	610	1179	0.0480	0.0028	0.0416	0.0023	0.0063	0.0001	41.4	2.3	40.7	0.6	44.0	1.6
YL1647-1	520	915	0.0515	0.0038	0.0440	0.0029	0.0064	0.0002	43.7	2.9	41.4	1.0	39.9	1.7
YL1656-9	492	1566	0.0477	0.0016	0.0429	0.0014	0.0065	0.0001	42.7	1.4	41.8	0.4	40.8	1.0
YL1656-17	566	1410	0.0467	0.0018	0.0420	0.0016	0.0065	0.0001	41.8	1.6	41.9	0.6	42.8	0.9

Table 2
Trace element compositions of zircons hosting magmatic sulfide melt inclusions.

Analyses	Ti	La	Ce	Pr	Nd	Sm	Eu	Gd	Tb	Dy	Ho	Er	Tm	Yb	Lu	Eu_N/Eu_N^*	$T_{Ti\text{-}in\text{-}zircon}$(°C)
YL1636-1	6.37	0.00	19	0.12	1.33	2.35	0.95	11.5	3.32	39	15	69	15	149	32	0.56	697
YL1636-2	1.87	0.00	42	0.13	1.28	3.61	1.47	17.8	5.40	71	27	134	29	296	66	0.56	607
ZK0812-389	3.40	0.00	49	0.05	1.20	2.32	1.49	14.5	4.64	53	21	100	23	235	54	0.78	649
YL1647-1	1.11	0.00	48	0.07	1.37	2.93	1.44	16.3	5.16	63	25	121	27	274	63	0.63	574
YL1656-9	2.06	0.37	25	0.12	1.21	1.73	0.77	9.02	2.91	35	15	75	18	206	49	0.59	619
YL1656-17	2.80	0.06	28	0.06	0.74	1.92	0.85	9.66	3.03	34	13	66	16	167	39	0.60	640

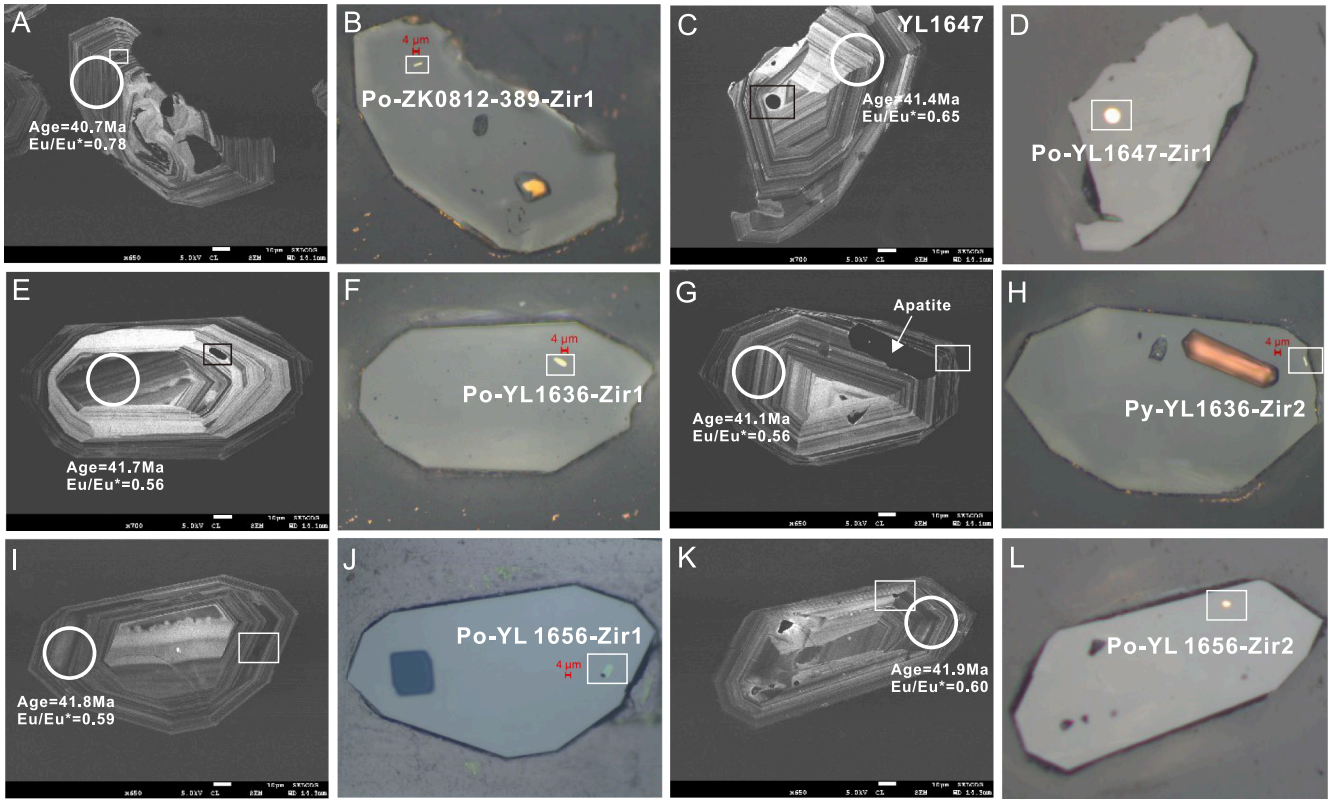

Fig. 4. Cathodoluminescence (CL) images and reflected light microphotographs of the SMIs and the sulfide-hosting zircons. Also shown are the U-Pb ages and Eu/Eu* values of the sulfide-hosting zircons.

Table 3
Compositions of magmatic sulfide minerals analyzed by EMPA (wt.%).

Analyses	Size	Ag	Au	Mo	Pd	Pt	S	Fe	Cu	Ni	Co	Total	Fe:S:Cu
Po-YL1636-Q4	8 μm × 13 μm	0.0	0.0	0.5	0.0	0.0	37.8	56.9	0.01	0.9	0.0	96.2	0.86:1:0
Po-YL1636-Q2	11 μm × 15 μm	0.0	0.0	0.4	0.0	0.0	38.6	58.0	0.00	0.9	0.1	98.0	0.86:1:0
Po-YL1647-Amp2	6 μm × 9 μm	0.0	0.0	0.4	0.0	0.0	38.6	57.9	0.01	0.5	0.1	97.6	0.85:1:0
Po-YL1647-Amp1	7 μm × 11 μm	0.0	0.1	0.3	0.0	0.0	38.8	59.7	0.16	0.2	0.1	99.4	0.88:1:0

Table 4
Compositions of magmatic sulfide minerals analyzed by EDS (wt.%).

Analyses	Size	Fe	S	Cu	Ni	Si	Zr	O	Ti	Total	Fe:S:Cu
Po-ZK0812-389-Zir1	2 μm × 5 μm	61.6	36.7	–	–	1.79	–	–	–	100	0.96:1:0
Po-ZK0812-389-Zir2	3 μm × 4 μm	61.2	38.8	–	–	–	–	–	–	100	0.91:1:0
Cpy-ZK0812-389-Zir3	1 μm × 2 μm	24.9	25.2	25.0	–	6.43	13.59	4.9	–	100	0.57:1:0.50
Po-YL1647-Zir1	5 μm × 6 μm	61.6	38.4	–	–	–	–	–	–	100	0.92:1:0
Po-YL1636-Zir1	3 μm × 7 μm	61.9	38.1	–	–	–	–	–	–	100	0.93:1:0
Py-YL1636-Zir2	1 μm × 5 μm	39.8	39.9	–	–	3.36	7.17	6.11	3.65	100	0.57:1:0
Po-YL1656-Zir1	5 μm × 10 μm	60.8	39.2	–	–	–	–	–	–	100	0.89:1:0
Po-YL1656-Zir2	6 μm × 8 μm	40.1	34.7	25.2	–	–	–	–	–	100	0.66:1:0.37

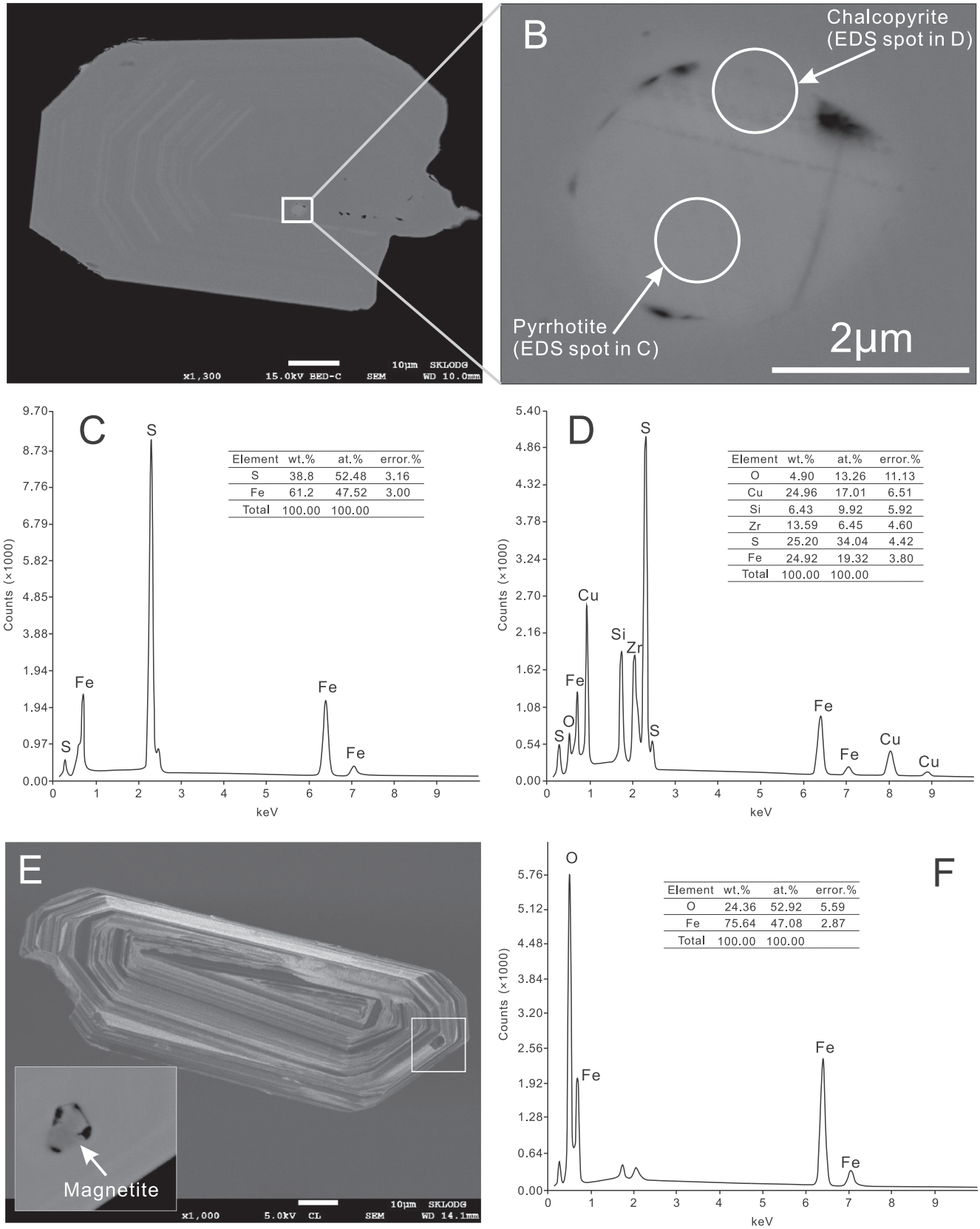

Fig. 5. Reflected light microphotograph (A) and back scattered electron (BSE) image (B) of a sulfide-hosting zircon. C-D. The EDS spectra and quantitative analyses of SMIs in Figure A-B. E. Cathodoluminescence image of a zircon crystal that hosts magnetite mineral inclusion. The inserted BSE image shows the occurrence of magnetite mineral inclusion. F. The EDS spectra and quantitative analyses of magnetite mineral inclusion in Figure E.

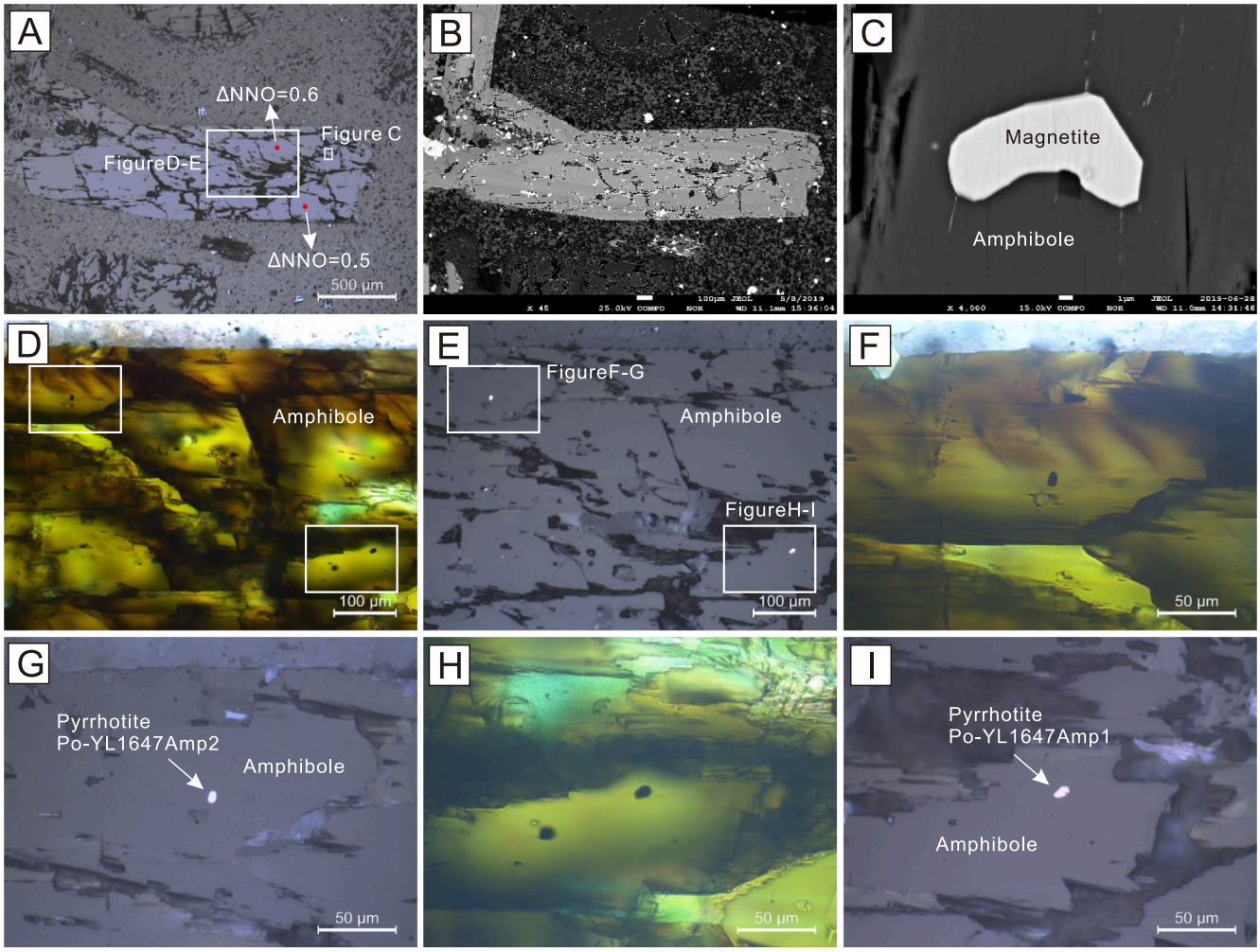

Fig. 6. Reflected light microphotograph (A) and BSE image (B) of the sulfide-hosting amphibole phenocryst. Also shown in A are the calculated ΔNNO values of the amphibole based on its EMPA major element compositions. C. Magnetite mineral inclusion in the amphibole phenocryst. D-I. Transmitted and reflected light microphotographs of the amphibole phenocryst, showing the occurrence of SMIs.

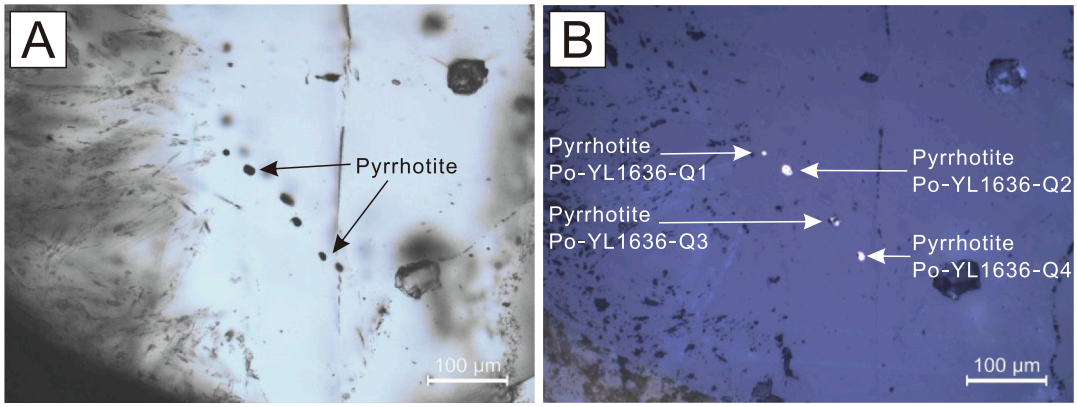

Fig. 7. Transmitted and reflected light microphotographs of the quartz phenocryst, showing the occurrence of a string of SMIs.

indicating that they are formed by fractionation of sulfide melts. The mineral association of pyrrhotite, pentlandite and chalcopyrite indicate that the sulfide melts might are mostly monosulfide melts (MSS) with magmatic origins.

The SMIs are generally oval or elongated in shape, and occur as globules or droplets within zircons, amphibole and quartz that are free of cracks (Figs. 4–7). The well-developed oscillatory zonings and hydrothermal-resistant feature of the hosting zircon, as well as the devoid of hydrothermal alteration in the subeconomic intrusions where sulfide-hosting amphibole and quartz were observed, suggesting that they were

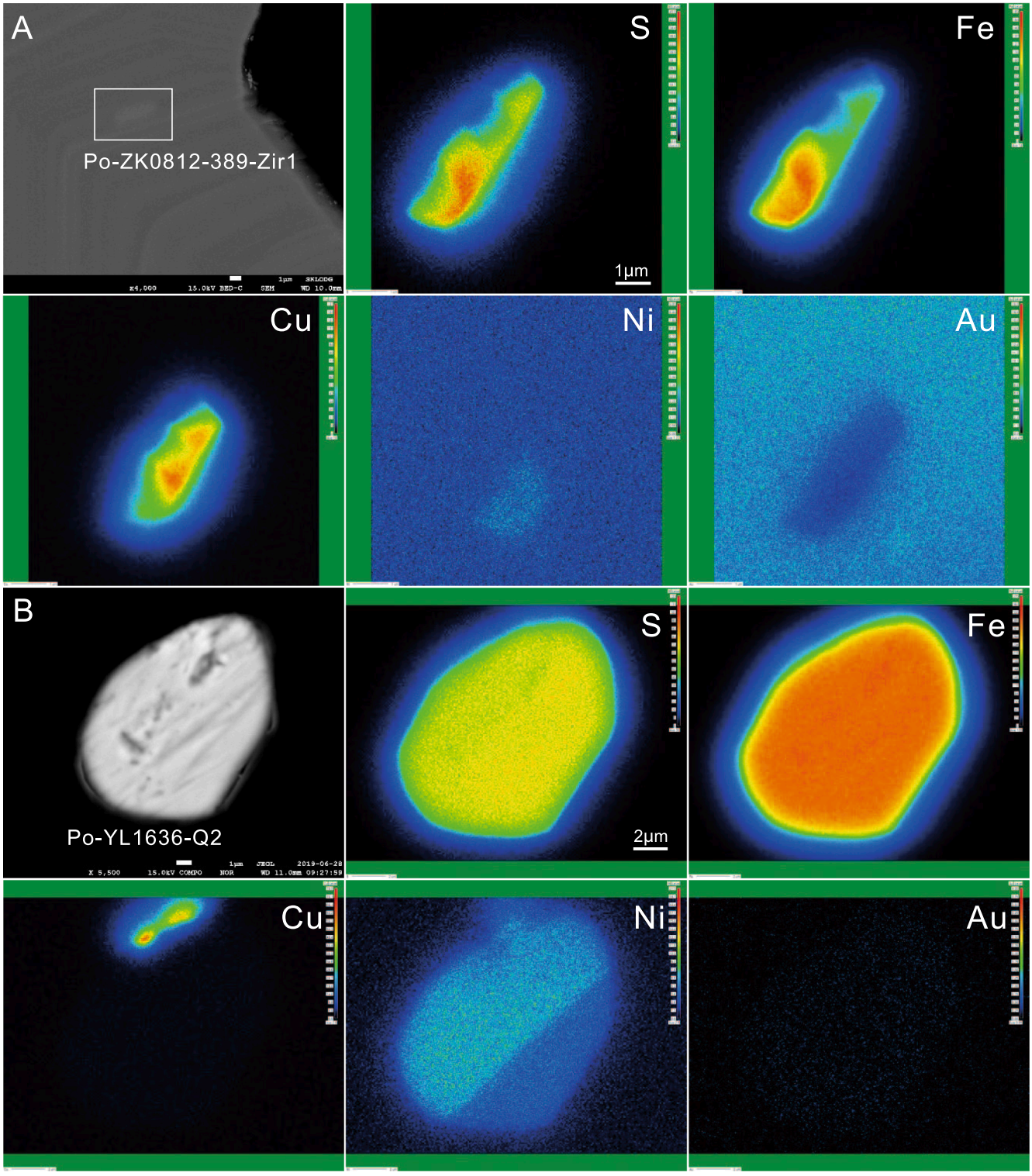

Fig. 8. Back scattered electron (BSE) image and element mapping results of the SMIs from sample ZK0812-389 (hosted in zircon) and sample YL1636 (hosted in quartz). Note that Cu and Ni are heterogeneously distributed in the pyrrhotite.

not formed in subsequent hydrothermal alteration processes. Therefore, we consider that the SMIs were of magmatic origin, and were initially trapped as sulfide melt inclusions during the growth of zircon, amphibole and quartz. This is similar to the cases at the Bingham and Escondida deposits (Halter et al., 2005; Hao et al., 2019).

In addition to the SMIs, we have also observed two magnetite mineral inclusions that were preserved in zircon and amphibole (Fig. 5E–F, 6C). Lack of cracks and good oscillatory zonings in CL images of hosting zircon also indicate a magmatic origin of such mineral inclusions. Therefore, mineral inclusion assemblages of both

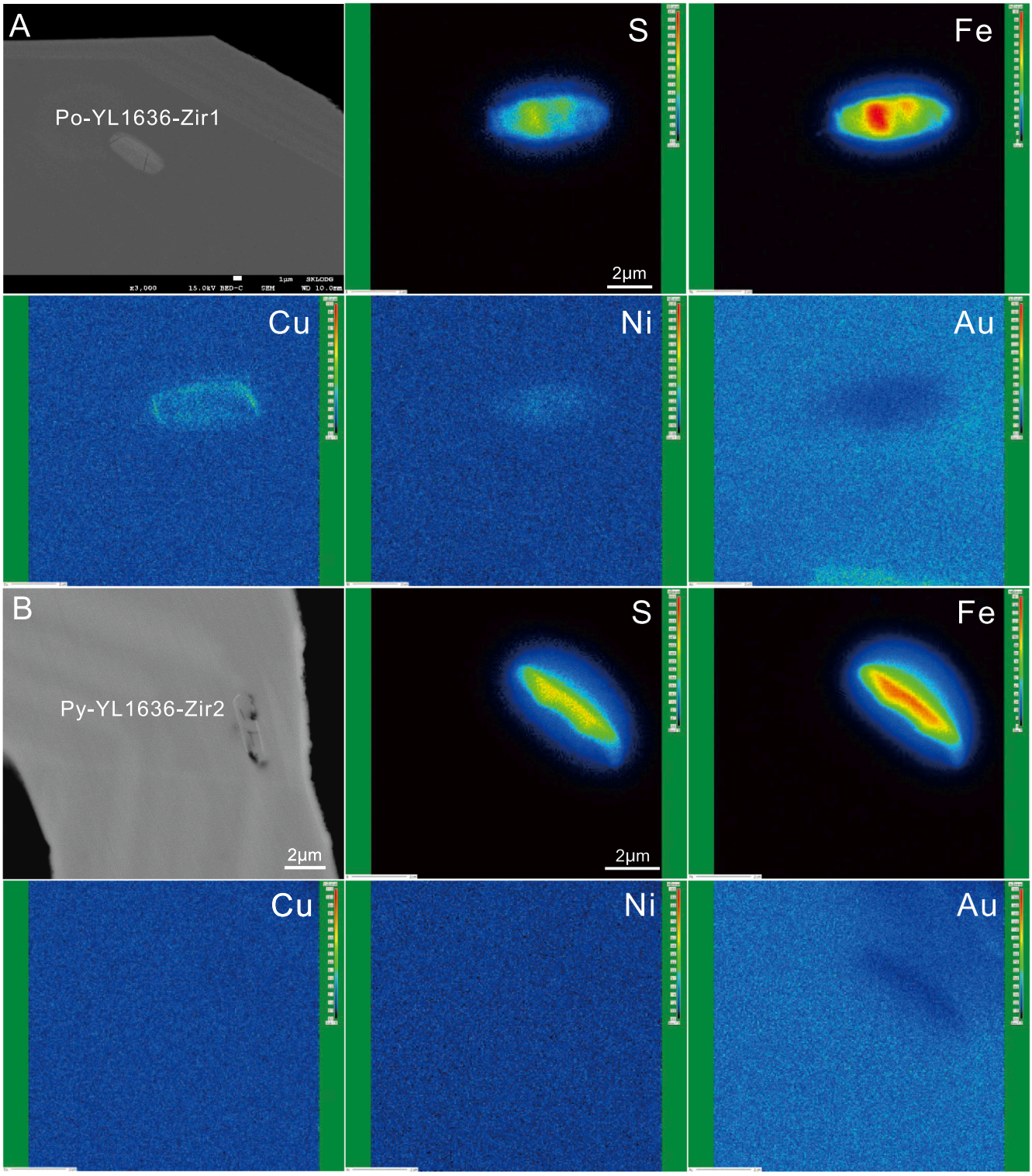

Fig. 9. Back scattered electron (BSE) image and element mapping results of the SMIs from sample YL1636 (hosted in zircon). The sulfide mineral inclusion in B has Fe:S:Cu ratio of 0.57:1:0, and is considered to be pyrite.

sulfide (pyrrhotite + pyrite + chalcopyrite) and oxides at Yulong are of magmatic origin, and might be possible to be formed at the same time.

6.2. *Timing of sulfide saturation and sulfide segregation*

Variations of PGE during magma differentiation (e.g., Pd vs. MgO) have been used to constrain the timing of sulfide saturation in porphyry Cu systems where co-magmatic mafic-intermediate volcanic rocks are preserved (Park et al., 2015; Hao et al., 2017). However, co-magmatic mafic-intermediate volcanic rocks are absent at Yulong, and the pre- and syn-mineralization intrusions have identical whole-rock major element geochemistry (e.g., similar MgO contents of ~1 wt% and SiO_2

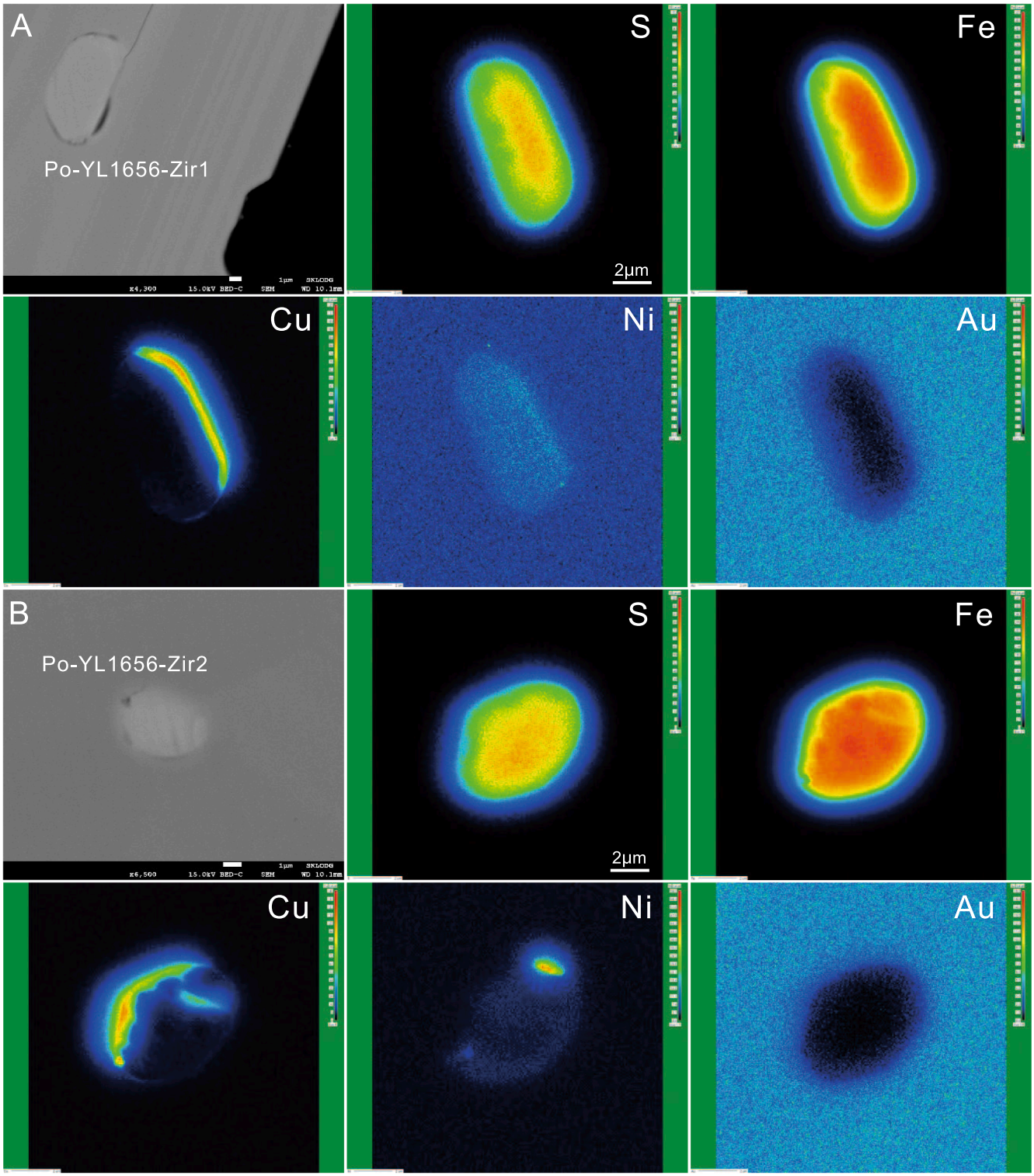

Fig. 10. Back scattered electron (BSE) image and element mapping results of the SMIs from sample YL1656 (hosted in zircon). Note the Cu-rich rims of these SMIs.

contents of ~69 wt%). As a consequence, it is difficult to constrain the timing of sulfide saturation by varying whole-rock MgO contents. Nonetheless, he occurrence of sulfide inclusions in early-crystallized phases (zircons and amphibole) implies that early sulfide saturation should have been reached.

Both barren and mineralized intrusions in the Yulong deposit have very low Pd (0.04 to 0.17 ppb) and Pt (0.19–0.60 ppb) contents, which are comparable to these of other porphyry Cu systems that have reached sulfide saturation during magma evolution (e.g. El Abra, Cocker et al., 2015), but are lower than those of porphyry Cu systems

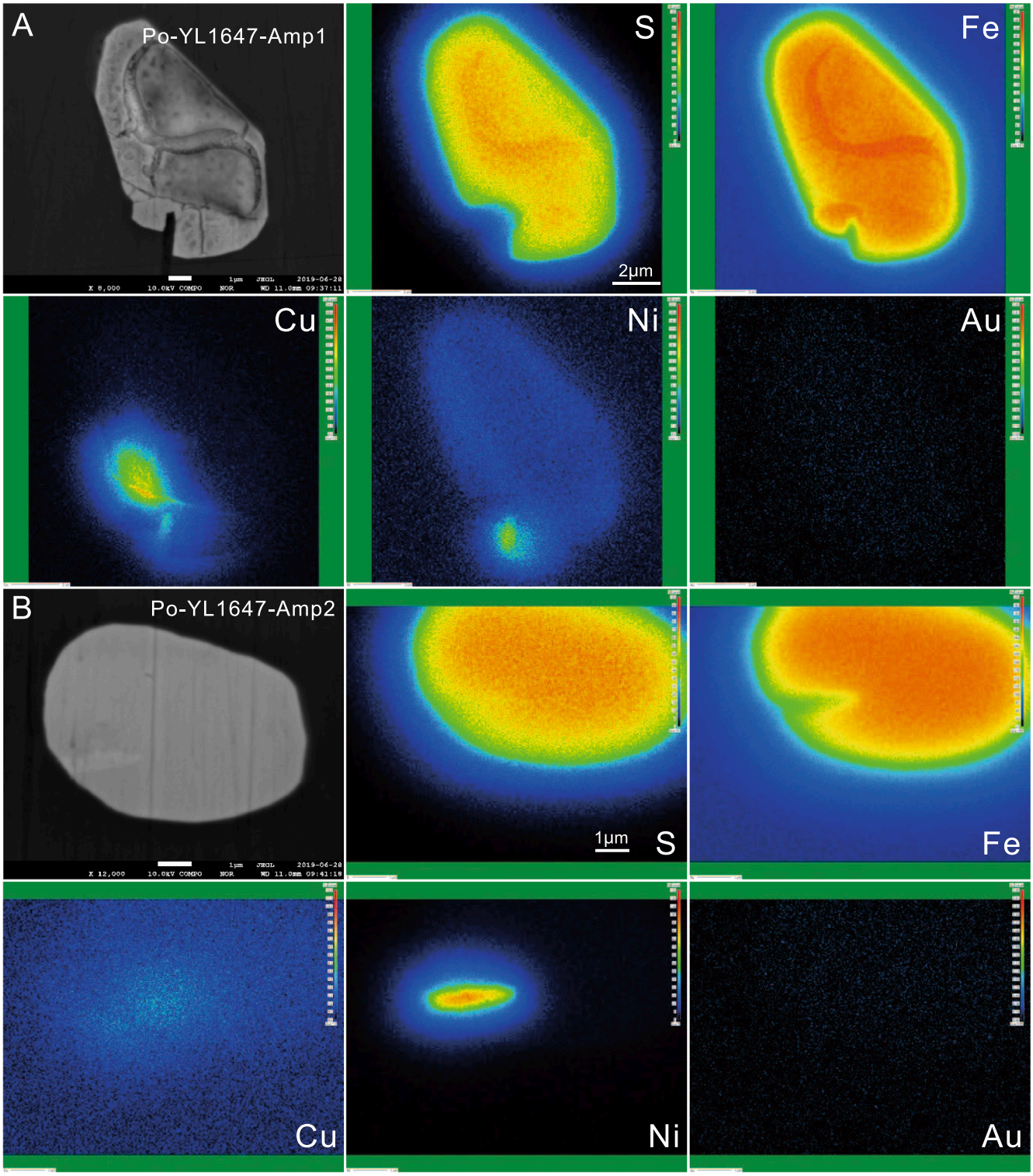

Fig. 11. Back scattered electron (BSE) image and element mapping results of the SMIs from sample YL1647 (hosted in amphibole). Cu and Ni are heterogeneously distributed in the SMI in A. The Ni-rich zone in B, containing no Cu and Fe, is considered to be pentlandite.

without early sulfide saturation (e.g. Pulang; Leng et al., 2018) (Fig. 13A–B) or intrusions experienced very late sulfide saturation just before fluid exsolution (such as Northparkes, Hao et al., 2017). Therefore, low PGE contents of the intrusions at Yulong also suggest that early sulfide saturation may have been reached and indicate that small amounts of sulfides have segregated from the magma, leading to the depletion PGEs in evolved magmas.

The SMI-hosting amphibole in this study has relatively higher crystallizing temperature (952°–953 °C) and pressure (5.2–5.3 kbar) than SMI-free amphibole from previous study (T = 774°–848 °C,

Table 5
Major element compositions and calculated crystallizing conditions of the amphibole phenocryst hosting magmatic sulfide melt inclusions.

Analyses	SiO_2	Al_2O_3	TiO_2	FeO	Cr_2O_3	MnO	MgO	CaO	Na_2O	K_2O	F	Cl	Total	$Mg^{\#}$	T (°C)	ΔNNO	logfO2	H_2Omelt (wt.%)	P (kbar)	Depth (km)
YL1646-4Amp-1	42.4	11.6	2.1	12.6	0	0.1	12.9	11.7	2.1	1.7	0.1	0.0	97.3	0.66	952	0.5	−10.5	3.9	5.3	20.2
YL1646-4Amp-2	42.6	11.6	2.1	12.2	0	0.1	13.2	11.8	2.1	1.6	0.1	0.0	97.4	0.67	953	0.6	−10.4	4.0	5.2	20.0

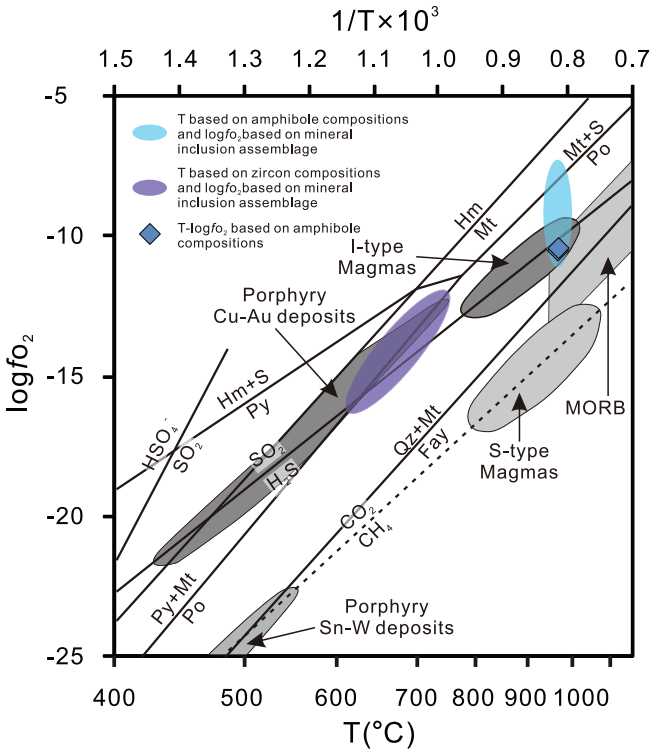

Fig. 12. Temperature vs. log fO_2 diagram showing the conditions of the Yulong porphyry system. The temperatures are quantitatively defined by the calculated crystallizing temperatures of zircon and amphibole that host SMIs, whereas the log fO_2 values are qualitatively defined by the mineral assemblage of the mineral inclusions (magnetite + pyrite + pyrrhotite) preserved in both zircon and amphibole. Modified from Richards (2015).

P = 1.9–3.3 kbar) (Huang et al., 2019b), possibly indicating that sulfide saturation probably has been reached in deeper magma chamber (20.0–20.2 km, assuming lithostatic pressure conditions and $\rho_{crust} = 2.7 \times 10^3$ kg/m^3) during the magma emplacement.

Previous studies have shown that extensive fluid exsolution, evidenced by elevated apatite F/Cl ratios, occurred during emplacement of the Yulong intrusion (Huang et al., 2019a). This, together with the sulfide inclusions in both pre-mineralization subeconomic intrusions and mineralized porphyry, indicates that the Yulong suite have reached sulfide saturation before fluid saturation.

6.3. Oxidation states of parental magmas

Zircon REE compositions can record oxidation and hydration states of the parent magmas. Zircons crystallized from oxidized fertile magmas generally have Eu_N/Eu_N^* values of > 0.4 (e.g., Ballard et al., 2002; Dilles et al., 2015; Lu et al., 2016). The sulfide-hosting zircons at Yulong have elevated Eu_N/Eu_N^* values of 0.56–0.78 (Fig. 4) that are similar to those of all intrusions in the Yulong magmatic suite (0.52–0.79; Huang et al., 2019a), indicating relatively high magmatic oxidation states of the Yulong magmas. High calculated ΔNNO value (+0.5) of the sulfide-hosting amphibole also supports the high oxygen fugacity nature (Fig. 6A). The high oxidation state at Yulong is also supported by the mineral inclusion assemblage of magnetite + pyrrhotite + pyrite + chalcopyrite. In the temperature vs. log fO_2 diagram, the above mineral assemblage in both zircon and amphibole indicates that the oxygen fugacity should be near the magnetite-pyrite/pyrrhotite buffer (Fig. 12), which is well above the fayalite-magnetite-quartz (FMQ) buffer, supporting oxidized nature of parental magmas.

It is noted that oxidation states of the magma during sulfide saturation increase from deep magma chamber (ΔNNO = +0.5 at 20.0–20.2 km; Table 5) via shallow magma chamber (ΔNNO = +0.6 to

Table 6
Whole-rock PGE compositions of the Yulong magmatic suite.

	Sample	Ir(ng/g)	Ru(ng/g)	Rh(ng/g)	Pt(ng/g)	Pd(ng/g)	ΣPGE	Pd/Pt
Mineralized Yulong intrusion	YL1522	0.02	0.12	0.04	0.10	0.32	0.59	3.30
	YL1523	0.01	0.09	0.01	0.04	0.20	0.36	4.64
	YL1524	0.10	0.11	0.03	0.17	0.33	0.74	1.86
	YL1525	0.01	0.14	0.04	0.11	0.26	0.57	2.28
	YL1525-4	0.01	0.11	0.03	0.13	0.41	0.69	3.16
	YL1525-7	0.01	0.10	0.03	0.12	0.21	0.47	1.82
	YL1528-2-1	0.01	0.12	0.02	0.06	0.19	0.39	3.24
	YL1528-2-2	0.01	0.12	0.04	0.11	0.34	0.62	3.24
	YL1530	0.01	0.12	0.01	0.13	0.40	0.67	2.97
	YL1549-2	0.03	0.15	0.02	0.16	0.29	0.64	1.82
	YL1552-2	0.02	0.10	0.01	0.09	0.22	0.44	2.51
	YL1552-3	0.03	0.14	0.04	0.09	0.60	0.89	7.03
Pre-mineralized intrusions	YL1636	0.04	0.14	0.03	0.08	0.53	0.82	6.32
	YL1648	0.03	0.18	0.01	0.04	0.33	0.58	7.70
	UMT-1(Measured)	6.5	8.1	7.1	140	102		
	UMT-1 (Certified*)	8.8	10.9	9.5	129	106		
	TDB-1 (Measured)	0.13	0.23	0.61	5.08	23.38		
	TDB-1 (Certified**)	0.15	0.3	0.7	5.8	22.4		

* Certified PGE values of UMT-1are from https://www.nrcan.gc.ca/mining-materials/certified-reference-materials/certificate-price-list/8043
** Certified PGE values of TDB-1are from Govindaraju (1994).

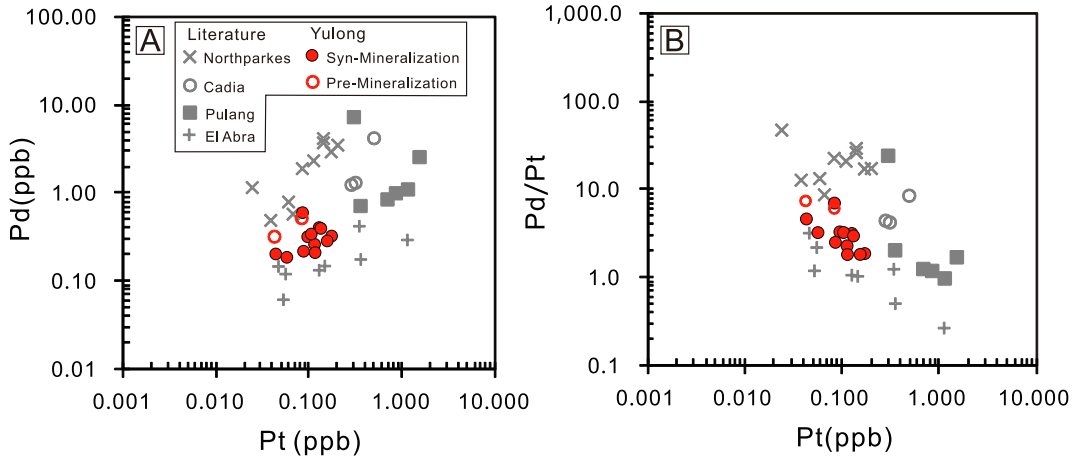

Fig. 13. Whole-rock Pd and Pt contents of the porphyry samples from the mineralized Yulong intrusion. A. Pd vs. Pt. B. Pd/Pt vs. Pt. Published PGEs contents of whole rock samples (MgO < 2.5 wt%) from other porphyrysystems are also shown (Pulang porphyry Cu-Au deposit, Leng et al., 2018; El Abra porphyry Cu deposit, Cocker et al., 2015; Cadia porphyry Au-Cu deposit, Lowczak et al., 2018; Northparkes porphyry Au-Cu deposit, Hao et al., 2017).

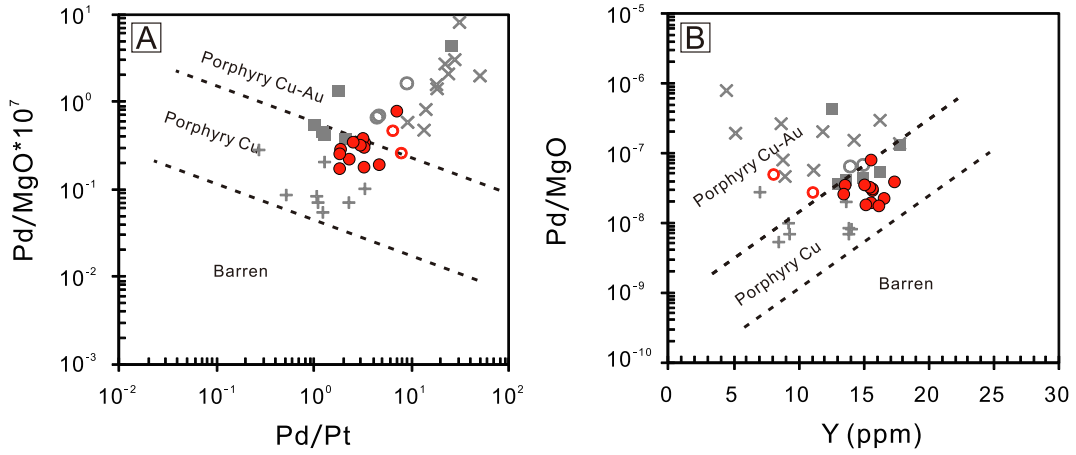

Fig. 14. Discrimination diagrams for barren, Cu-only, and Cu-Au porphyries based PGE contents of porphyry samples with MgO < 2.5 wt%. The Yulong samples were plotted in the porphyry Cu fields in both diagrams. MgO contents (wt.%) of corresponding Yulong samples are from Huang et al. (2019a, b). Data sources of other porphyry systems are the same as Fig. 13. (A) Pd/MgO*10^7 vs. Pd/Pt (Park et al., 2018). (B) Pd/MgO vs. Y (Hao et al., 2019). Legend is the same as those in Fig. 13.

+1.5 at 7.1–12.5 km) to the porphyritic stock (ΔNNO = +1.9 to +2.3 at 4.0–5.6 km) (Huang et al., 2019b), which is consistent with early sulfide saturation in deep magma chamber.

6.4. Possible influence of early sulfide saturation on porphyry mineralization

As demonstrated above, the magmatic oxidation states at the time of sulfide saturation at Yulong are still high at > ΔNNO +0.5 (Figs. 4, 6, 12). Experimental studies have shown that under oxidized conditions (ΔFMQ +1 to +2, corresponding to ΔNNO +0.3 to +1.3), most of the sulfur in the magma would exist as SO_4^{2-}, but minor reduced S^{2-} could still be present due to the dynamic-balanced reaction of $S^{2-}_{melt} + 2O_2 = SO4^{2-}_{melt}$ (Jugo et al., 2005, 2010). We consider that the SMIs at Yulong are probably formed by combination of reduced S^{2-} and Fe (and Cu) or by locally contamination of reduced country rocks. Small degrees of sulfide saturation have been gained and small amount of sulfides have segregated from magmas. These small amounts of sulfides are considered unlikely and insufficient to extract a large amount of the ore-forming metals (> 6Mt Cu) from the magma. On the contrary, early sulfide saturation and segregation would have negative effects on porphyry mineralization (Richards, 2003, 2011, 2015; Audétat and Pettke, 2006).

The Yulong deposit is characterized by Au-poor porphyry Cu-Mo mineralization (Tibet Yulong Copper Co., Ltd., 2009). It has been suggested that Au-poor porphyry Cu mineralization could be the product of origination from a Au-poor source (Mathur et al., 2000) or removal of Au by sulfide segregation (Park et al., 2015). However, the recent discovery of the Bada porphyry Au deposit in the Yulong belt suggest that the source region of the Yulong belt is likely Au-rich (Zhang et al., 2019 and the reference therein), precluding the idea of origin of Au-poor source.

Due to very different partition coefficients of PGE, Au and Cu between sulfide melts and silicate magmas, early sulfide saturation would have highly variable effects on changing the abundance of these ore-forming metals in evolved magmas. For Au and PGEs, the partition coefficients of Au and PGEs between sulfides and silicate melts are extremely large ($D_{Au} \approx 10^4$, $D_{Pd} \approx 2 \times 10^5$; Mungall and Brenan, 2014). Thus, even small amounts of early sulfide saturation could remarkable lower their concentrations in evolving magma. In contrast, the partition coefficients of Cu between sulfides and silicate melts ($D_{Cu} \approx 1300$; Ripley et al., 2002) are about one to two orders of magnitude lower than Au and PGEs. Therefore, small amounts of early sulfide saturation would not be sensitive in decreasing Cu contents in the evolving magma (c.f. Park et al., 2015; Cocker et al., 2015; Hao et al., 2017). Variable Cu contents in most SMIs (Fig. 5D, 8–11; Tables 3 and 4) indicate that Au and PGEs (much more chalcophile) would be probably much more seriously affected. Thus, we speculate that small amounts of sulfide saturation at Yulong may have depleted the evolving magma in most PGE and Au but only small proportion of Cu, leading to the formation of the Yulong Au-poor porphyry Cu deposit (Fig. 14).

Recent studies have shown that platinum-group element geochemistry could also be used to constrain whether a porphyry system is fertile or not (e.g., barren, Cu-only, or Cu-Au, Park et al., 2015, 2018; Cocker et al., 2015; Hao et al., 2017; Lowczak et al., 2018). Two empirical diagrams for low-MgO porphyry samples (< 2.5 wt%) elsewhere, i.e., Pd/MgO*10^7 vs. Pd/Pt (Park et al., 2018) and Pd/MgO vs. Y (Hao et al., 2019), could be effective in discriminating porphyry systems with variable metal mineralization potentials. In these diagrams, higher Pd/MgO ratio is regarded as later and smaller fraction of sulfide precipitation (Hao et al., 2019), the Pd/Pt ratio is used as a vector of amount of fractional crystallization before sulfide saturation (Park et al., 2018), and whole-rock Y content is used to evaluate magmatic water contents (Hao et al., 2019). Samples from pre-mineralization intrusions (Y1 and Y3) at Yulong plot near the boundary between porphyry Cu and Cu-Au fields, whereas samples from the mineralized Yulong intrusion plot in the porphyry Cu fields in both of these two diagrams, supporting that early sulfide saturation may have depleted the evolving magma with most PGE and Au, but only part of the Cu. Therefore, early sulfide saturation and segregation result in the Yulong an Au-poor porphyry Cu deposit.

7. Conclusions

Magmatic sulfide melt inclusions have been observed in zircon, amphibole and quartz from pre- and syn-mineralization intrusions at the Yulong porphyry Cu deposit, suggesting early sulfide saturation during magmatic evolution. These SMIs generally occur as globules or droplets, and are composed mainly of pyrrhotite with minor pyrite, chalcopyrite and pentlandite. Magnetite mineral inclusions are also observed in zircon and amphibole. The above mineral assemblage, combined with high Eu/Eu* ratios of the hosting zircons and calculated ΔNNO values of the hosting amphibole, indicates relatively high magmatic oxygen fugacity at the time of sulfide saturation.

Small amounts of sulfide saturation have depleted most PGE and Au but minor Cu in the evolving magmas so that the evolving magmas and ore-forming fluids exsolved afterwards are depleted in Au, producing the Cu-rich and Au-poor Yulong deposit.

Declaration of Competing Interest

The authors declare that they have no known competing financial interests or personal relationships that could have appeared to influence the work reported in this paper.

Acknowledgements

This study was jointly funded by the Natural Science Foundation of China (91955209, 41873052), the Strategic Priority Research Program (B) of the Chinese Academy of Sciences (XDB18000000), the “CAS Hundred Talents” Project to Jian-Feng Gao, Team of the Belt and Road of the Chinese Academy of Sciences, China, and 100 Innovative Talents of Guizhou province to Xian-Wu Bi. The authors thank Xing-Chun Zhang and Shen-Tai Liu for the help during field investigation, and Xiang Li and Yan-Wen Tang for the assistance in EMPA and LA-ICP-MS analyses. The first author benefited greatly from discussion with Dr. Hong-Da Hao during his visit in Laurentian University, Canada. Two anonymous reviewers and editors are much appreciated for their critical and constructive comments on this paper.

Appendix A

Fig. A1

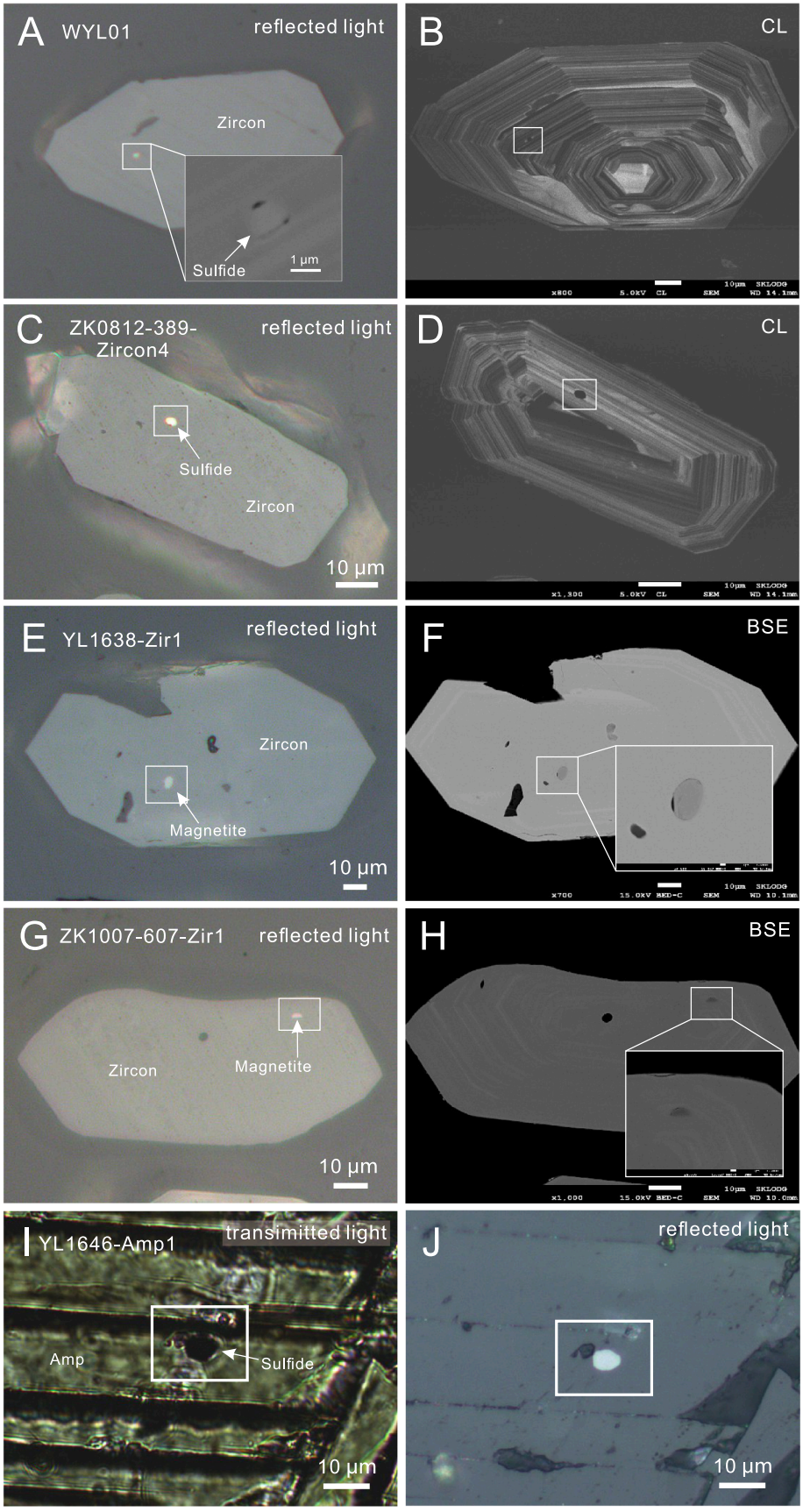

Fig. A1. Microphotographs of the SMIs from zircon and amphibole phenocrysts.

Appendix B. Supplementary data

Supplementary data to this article can be found online at https://doi.org/10.1016/j.oregeorev.2020.103644.

References

Audétat, A., Pettke, T., 2006. Evolution of a porphyry-Cu mineralized magma system at Santa Rita, New Mexico (U.S.A.). J. Petrol. 47, 2021–2046.

Ballard, J.R., Palin, M.J., Campbell, I.H., 2002. Relative oxidation states of magmas inferred from Ce(IV)/Ce(III) in zircon: Application to porphyry copper deposits of northern Chile. Contrib. Miner. Petrol. 144, 347–364.

Bi, X.W., Hu, R.Z., Peng, J.T., Wu, K.X., Su, W.C., Zhan, X.Z., 2005. Geochemical characteristics of the Yao'an and Machangqing alkaline-rich intrusions. Acta Petrol. Sinica 21, 113–124 (in Chinese with English abstract).

Bi, X.W., Hu, R.Z., Hanley, J.J., Mungall, J.E., Peng, J.T., Shang, L.B., Wu, K.X., Shuang, Y., Li, H.L., Hu, X.Y., 2009. Crystallisation conditions (T, P, fO2) from mineral chemistry of Cu- and Au-mineralised alkaline intrusions in the Red River-Jinshajiang alkaline igneous belt, western Yunnan Province, China. Mineral. Petrol. 96, 43–58.

Cao, M.J., Hollings, P., Cooke, D.R., Evans, N.J., McInnes, B.I.A., Qin, K.Z., Li, G.M., Sweet, G., Baker, M., 2018. Physicochemical processes in the magma chamber under the Black Mountain porphyry Cu-Au deposit (Philippines): insights from mineral chemistry and implications for mineralization. Econ. Geol. 113, 63–82.

Chang, J., Li, J.W., Selby, D., Liu, J.C., Deng, X.D., 2017. Geological and chronological constraints on the long-lived Eocene Yulong porphyry Cu-Mo deposit, eastern Tibet: implications for the lifespan of giant porphyry Cu deposits. Econ. Geol. 112, 1719–1746.

Cocker, H.A., Valente, D.L., Park, J.W., Campbell, I.H., 2015. Using platinum group elements to identify sulfide saturation in a porphyry Cu system: the El Abra porphyry Cu deposit, Northern Chile. J. Petrol. 56, 2491–2514.

Deng, J., Wang, Q.F., Li, G.J., Hou, Z.Q., Jiang, C.Z., Danyushevsky, L., 2015. Geology and genesis of the giant Beiya porphyry-skarn gold deposit, northwestern Yangtze block, China. Ore Geol. Rev. 70, 457–485.

Dilles, J.H., Kent, A.J., Wooden, J.L., Tosdal, R.M., Koleszar, A., Lee, R.G., Farmer, L.P., 2015. Zircon compositional evidence for sulfur-degassing from ore-forming arc magmas. Econ. Geol. 110, 241–251.

Gao, J.-F., Zhou, M.-F., Qi, L., Chen, W.T., Huang, X.-W., 2015. Chalcophile elemental compositions and origin of the Tuwu porphyry Cu deposit, NW China. Ore Geol. Rev. 66, 403–421.

Govindaraju, K., 1994. Compilation of working values and sample description for 383 Geostandards. Geostandard. Neswlett. 18, 331–334, p 53.

Guo, L.G., Liu, Y.P., Xu, W., Zhang, X.C., Qin, K.Z., Li, T.S., Shi, Y.R., 2006. Constraints to the mineralization age of the Yulong porphyry copper deposit from SHRIMP U-Pb zircon data in Tibet. Acta Petrol. Sinica 22, 1009–1016.

Halter, W.E., Heinrich, C.A., Pettke, T., 2005. Magma evolution and the formation of porphyry Cu–Au ore fluids: evidence from silicate and sulfide melt inclusions. Miner. Deposita 39, 845–863.

Hao, H.D., Campbell, I.H., Park, J.W., Cooke, D.R., 2017. Platinum-group element geochemistry used to determine Cu and Au fertility in the Northparkes igneous suites, New South Wales, Australia. Geochim. Cosmochim. Acta 216, 372–392.

Hao, H.D., Campbell, I.H., Richards, J.P., Sakaguchi, C., Nakamura, E., 2019. Platinum-Group Element Geochemistry of the Escondida Igneous Suites, Northern Chile: Implications for Ore Formation. J. Petrol. 60, 487–514.

He, W.Y., Mo, X.X., He, Z.H., White, N.C., Chen, J.B., Yang, K.H., Wang, R., Yu, X.H., Dong, G.C., Huang, X.F., 2015. The geology and mineralogy of the Beiya skarn gold deposit in Yunnan, southwest China. Econ. Geol. 110, 1625–1641.

Hou, Z.Q., Ma, H.W., Khin, Z., Zhang, Y.Q., Wang, M.J., Wang, Z., Pan, G.T., Tang, R.L., 2003. The Himalayan Yulong porphyry copper belt: Product of large-scale strike-slip faulting in eastern Tibet. Econ. Geol. 98, 125–145.

Hou, Z.Q., Zeng, P.S., Gao, Y.F., Du, A.D., Fu, D.M., 2006. Himalayan Cu-Mo-Au mineralization in the eastern Indo-Asian collision zone: Constraints from Re-Os dating of molybdenite. Miner. Deposita 41, 33–45.

Hou, Z.Q., Xie, Y.L., Xu, W.Y., Li, Y.Q., Zhu, X.K., Khin, Z., Beaudoin, G., Rui, Z.Y., Wei, H.A., Luobu, C.R., 2007. Yulong deposit, eastern Tibet: A high-sulfidation Cu-Au porphyry copper deposit in the eastern Indo-Asian collision zone. Int. Geol. Rev. 49, 235–258.

Hu, R.Z., Burnard, P.G., Bi, X.W., Zhou, M.F., Pen, J.T., Su, W.C., Wu, K.X., 2004. Helium and argon isotope geochemistry of alkaline intrusion-associated gold and copper deposits along the Red River-Jinshajiang fault belt, SW China. Chem. Geol. 203, 305–317.

Huang, M.L., Bi, X.W., Gao, J.F., Xu, L.L., Xiao, J.F., Liu, S.T., Wang, X.S., Zhou, T., 2019c. Sulfur and lead isotopic variations in the giant Yulong porphyry Cu (Mo-Au) deposit from the eastern Tibetan Plateau: Implications for origins of S and Pb, and metal precipitation. J. Geochem. Explor. 197, 70–83.

Huang, M.L., Bi, X.W., Hu, R.Z., Gao, J.F., Xu, L.L., Zhu, J.J., Shang, L.-B., 2019b. Geochemistry, *in-situ* Sr-Nd-Hf-O isotopes, and mineralogical constraints on origin and magmatic-hydrothermal evolution of the Yulong porphyry Cu-Mo deposit, Eastern Tibet. Gondwana Res. 76, 98–114.

Huang, M.L., Bi, X.W., Richards, J.P., Hu, R.Z., Xu, L.L., Gao, J.F., Zhu, J.J., Zhang, X.C., 2019a. High water contents of magmas and extensive fluid exsolution during the formation of the Yulong porphyry Cu-Mo deposit, eastern Tibet. J. Asian Earth Sci. 176, 168–183.

Jiang, X.J., Li, W.C., 2019. Unpublished oral presentation in: the Ninth National Symposium about Metallogenic Theory and Prospecting Method, Nanjing, China, December 13-16, 2019.

Jiang, Y.H., Jiang, S.Y., Ling, H.F., Dai, B.Z., 2006. Low-degree melting of a metasomatized lithospheric mantle for the origin of Cenozoic Yulong monzogranite porphyry, east Tibet: Geochemical and Sr-Nd-Pb-Hf isotopic constraints. Earth Planet. Sci. Lett. 241 (3–4), 617–633.

Jugo, P.J., Luth, R.W., Richards, J.P., 2005. Experimental data on the speciation of sulfur as a function of oxygen fugacity in basaltic melts. Geochim. Cosmochim. Acta 69, 497–503.

Jugo, P.J., Wilke, M., Botcharnikov, R.E., 2010. Sulfur K-edge XANES analysis of natural and synthetic basaltic glasses: Implications for S speciation and S content as function of oxygen fugacity. Geochim. Cosmochim. Acta 74, 5926–5938.

Keith, J.D., Whitney, J.A., Hattori, K., Ballantyne, G.H., Christiansen, E.H., Barr, D.L., Cannan, T.M., Hook, C.J., 1997. The role of magmatic sulfides and mafic alkaline magmas in the Bingham and Tintic mining districts, Utah. J. Petrol. 38, 1679–1690.

Lee, C.-T.A., Luffi, P., Chin, E.J., Bouchet, R., Dasgupta, R., Morton, D.M., Le Roux, V., Yin, Q.Z., Jin, D., 2012. Copper systematics in arc magmas and implications for crust-mantle differentiation. Science 336, 64–68.

Leng, C.-B., Gao, J.-F., Chen, W.T., Zhang, X.-C., Tian, Z.-D., Guo, J.-H., 2018. Platinum-group elements, zircon Hf-O isotopes, and mineralogical constraints on magmatic evolution of the Pulang porphyry Cu-Au system, SW China. Gondwana Res. 62, 163–177.

Li, J.X., Qin, K.Z., Li, G.M., Cao, M.J., Xiao, B., Chen, L., Zhao, J.X., Evans, N.J., McInnes, B.I.A., 2012. Petrogenesis and thermal history of the Yulong porphyry copper deposit, eastern Tibet: Insights from U-Pb and U-Th/He dating, and zircon Hf isotope and trace element analysis. Mineral. Petrol. 105, 201–221.

Liang, H.Y., Campbell, I.H., Allen, C., Sun, W.D., Liu, C.Q., Yu, H.X., Xie, Y.W., Zhang, Y.Q., 2006. Zircon Ce^{4+}/Ce^{3+} ratios and ages for Yulong ore-bearing porphyries in eastern Tibet. Miner. Deposita 41, 152–159.

Lin, B., Wang, L., Tang, J., Song, Y., Cao, H., Baker, M.J., Zhang, L., Zhou, X., 2018. Geology, geochronology, geochemical characteristics and origin of Baomai porphyry Cu (Mo) deposit, Yulong Belt, Tibet. Ore Geol. Rev. 92, 186–204.

Liu, Y.S., Hu, Z.C., Gao, S., Günther, D., Xu, J., Gao, C.G., Chen, H.H., 2008. In-situ analysis of major and trace elements of anhydrous minerals by LA-ICP-MS without applying an internal standard. Chem. Geol. 257, 34–43.

Liu, Y.S., Gao, S., Hu, Z.C., Gao, C.G., Zong, K.Q., Wang, D.B., 2010. Continental and oceanic crust recycling-induced melt-peridotite interactions in the trans-north China Orogen: U-Pb dating, Hf isotopes and trace elements in zircons from mantle xenoliths. J. Petrol. 51, 537–571.

Lowczak, J.N., Campbell, I.H., Cocker, H., Park, J.W., Cooke, D.R., 2018. Platinum-group element geochemistry of the Forest Reef Volcanics, southeastern Australia: implications for porphyry Au-Cu mineralization. Geochim. Cosmochim. Acta 220, 385–406.

Lu, Y.J., Loucks, R.R., Fiorentini, M., McCuaig, T.C., Evans, N.J., Yang, Z.M., Hou, Z.Q., Kirkland, C.L., Parra-Avila, L.A., Kobussen, A., 2016. Zircon compositions as a pathfinder for Cu ± Mo ± Au deposits. Society of Economic Geologists Special Publication 19, 329–347.

Mathur, R., Ruiz, J., Titley, S., Gibbins, S., Margotomo, W., 2000. Different crustal sources for Au-rich and Au-poor ores of the Ggrasberg Cu–Au porphyry deposit. Earth and Planetary Science Letter 183, 7–14.

Mo, X.X., Hou, Z.Q., Niu, Y.L., Dong, G.C., Qu, X.M., Zhao, Z.D., Yang, Z.M., 2007. Mantle contributions to crustal thickening during continental collision: evidence from Cenozoic igneous rocks in southern Tibet. Lithos 96 (1), 225–242.

Mungall, J.E., Brenan, J.M., 2014. Partitioning of platinum-group elements and Au between sulfide liquid and basalt and the origins of mantle-crust fractionation of the chalcophile elements. Geochim. Cosmochim. Acta 125, 265–289.

Mungall, J.E., Brenan, J.M., Godel, B., Barnes, S.J., Gaillard, F., 2015. Transport of metals and sulphur in magmas by flotation of sulphide melt on vapour bubbles. Nat. Geosci. 8, 216–219.

Nadeau, O., Williams-Jones, A.E., Stix, J., 2010. Sulphide magma as a source of metals in arc-related magmatic hydrothermal ore fluids. Nat. Geosci. 3, 501–505.

Park, J.W., Campbell, I.H., Kim, J., Moon, J.W., 2015. The role of late sulfide saturation in the formation of a Cu- and Au-rich magma: insights from the platinum group element geochemistry of Niuatahi-Motutahi lavas, Tonga Rear Arc. J. Petrol. 56, 59–81.

Park, J.W., Campbell, I.H., Malaviarachchi, S.P., Cocker, H., Hao, H.-D., Kay, S. M., 2018. Chalcophile element fertility and the formation of porphyry Cu6Au deposits. Mineralium Deposita, 1–14. Doi: 10.1007/s00126-018-0834-0.

Qi, L., Gao, J.F., Huang, X.W., Hu, J., Zhou, M.F., Zhong, H., 2011. An improved digestion technique for determination of platinum group elements in geological samples. J. Anal. At. Spectrom. 26, 1900–1904.

Richards, J.P., 2003. Tectono-magmatic precursors for porphyry Cu-(Mo-Au) deposit formation. Econ. Geol. 98, 1515–1533.

Richards, J.P., 2015. The oxidation state, and sulfur and Cu contents of arc magmas: Implications for metallogeny. Lithos 233, 27–45.

Ridolfi, F., Renzulli, A., Puerini, M., 2010. Stability and chemical equilibrium of amphibole in calc-alkaline magmas: an overview, new thermobarometric formulations and application to subduction-related volcanoes. Contributions to amphibole in calc-alkaline magmas: an overview, new thermobarometric formulations and application to subduction-related volcanoes. Contributions to Minerology and Petrology 160, 45–66.

Ripley, E.M., Brophy, J.G., Li, C.S., 2002. Copper solubility in a basaltic melt and sulfide liquid/silicate melt partition coefficients of Cu and Fe. Geochim. Cosmochim. Acta 66, 2791–2800.

Stavast, W.J.A., Keith, J.D., Christiansen, E.H., Dorais, M.J., Tingey, D., 2006. The fate of magmatic sulfides during intrusion or eruption, Bingham and Tintic districts, Utah. Econ. Geol. 101, 329–345.

Tang, R.L., Luo, H.S., 1995. The geology of Yulong porphyry copper (molybdenum) ore belt. Geological Publishing House, Xizang (Tibet): Beijing, pp. 157.

Tang, J.X., Wang, C.H., Qu, W.J., Du, A.D., Ying, L.J., Gao, Y.M., 2009. Re-Os isotopic dating of molybdenite from the Yulong porphyry copper-molybdenum deposit in Tibet and its metallogenic significance. Rock and Mineral Analysis 28, 215–218 (in Chinese with English abstract).

Tibet Yulong Copper Co., Ltd., 2009. Yulong Copper Polymetallic Deposit Exploration Report. Jomda County, Tibet.

Wang, C.H., Tang, J.X., Chen, J.P., Hao, J.H., Gao, Y.M., Liu, Y.W., Fan, T., Zhang, Q.Z., Ying, L.J., Chen, Z.J., 2009. Chronological research of Yulong copper-molybdenum porphyry deposit. Acta Geol. Sinica 83, 1445–1455 (in Chinese with English abstract).

Wang, C.H., Tang, J.X., Hou, K.J., Gao, Y.M., Chen, J.P., Hao, J.H., Ying, L.J., Zhang, Q.Z., Liu, Y.W., Fan, T., 2011. Hf isotopic characteristics of Yulong copper-molybdenum porphyry deposit in Tibet and their geological significance. Mineral Deposits 30, 292–304 (in Chinese with English abstract).

Wang, J.H., Yin, A., Harrison, T.M., Grove, M., Zhang, Y.Q., Xie, G.H., 2001. A tectonic model for Cenozoic igneous activities in the eastern Indo-Asian collision zone. Earth Planet. Sci. Lett. 88, 123–133.

Watson, E.B., Wark, D.A., Thomas, J.B., 2006. Crystallization thermometers for zircon and rutile. Contrib. Miner. Petrol. 151, 413–433.

Wiedenbeck, M., Allé, P., Corfu, F., Griffin, W.L., Meier, M., Oberli, F., Quadt, A.V., Roddick, J.C., Spiegel, W., 1995. Three natural zircon standards for U-Th-Pb, Lu-Hf, trace element and REE analyses. Geostand. Geoanal. Res. 19, 1–23.

Wilkinson, J.J., 2013. Triggers for the formation of porphyry ore deposits in magmatic arcs. Nat. Geosci. 6, 917–925.

Xu, L.L., Bi, X.W., Hu, R.Z., Zhang, X.C., Su, W.C., Qu, W.J., Hu, Z.C., Tang, Y.Y., 2012. Relationships between porphyry Cu-Mo mineralization in the Jinshajiang-Red River metallogenic belt and tectonic activity: constraints from zircon U-Pb and molybdenite Re-Os geochronology. Ore Geol. Rev. 48, 460–473.

Xu, L.L., Bi, X.W., Hu, R.Z., Qi, Y.Q., Tang, Y.Y., Wang, X.S., Zhu, J.-J., 2016. Redox states and genesis of magmas associated with intra-continental porphyry Cu-Au mineralization within the Jinshajiang-Red River alkaline igneous belt, SW China. Ore Geol. Rev. 73, 330–345.

Yang, Z.M., Cooke, D.R., 2019. Porphyry Copper Deposits in China. Society of Economic Geologists Special Publication, vol. 22, pp. 133–187.

Yang, Z.M., Hou, Z.Q., Xu, J.F., Bian, X.F., Wang, G.R., Yang, Z.S., Tian, S.H., Liu, Y.C., Wang, Z.L., 2014. Geology and origin of the post-collisional Narigongma porphyry Cu-Mo deposit, southern Qinghai, Tibet. Gondwana Res. 26 (2), 536–556.

Zhang, D.H., Audétat, A., 2017. What caused the formation of the giant Bingham Canyon porphyry Cu-Mo-Au deposit? Insights from melt inclusions and magmatic sulfides. Econ. Geol. 112, 221–244.

Zhang, H., Wang, B.D., Yu, Y.S., He, H., Xiao, P., Wang, F.M., 2019. Petrogenesis of the Riqu Granodiorite Porphyry in Southern Yulong Porphyry Copper Belt: Constraints from Zircon U-Pb Geochronology and Whole-Rock Geochemistry. Bull. Mineral., Petrol. Geochem. 38, 379–394 (in Chinese with English abstract).

Zhang, Y.Q., Xie, Y.W., 1997. Geochronology of Ailaoshan-Jinshajiang alkali-rich intrusive rocks and their Sr and Nd isotopic characteristics. Sci. China, Ser. D Earth Sci. 40, 524–529 (in Chinese with English abstract).